A Neisseria gonorrhoeae colony under shear: Viscoelasticity of an active network

Master's Thesis in Physics

Presented by

Leander Self

December 3rd, 2020

Institute for Theoretical Physics 1
Friedrich-Alexander University Erlangen-Nürnberg

Supervisor: Prof. Dr. Michael Schmiedeberg

Contents

1 Introduction

One of the most prevalent sexually transmitted diseases, gonorrhea, is caused by the bacterium Neisseria gonorrhoeae [1]. Cells of this species use retractable appendages, called pili, in the process of colonisation and infection. They serve several purposes, one of them being the formation of bacterial communities [2]. The resulting biofilms and their precursors, microcolonies, are a means of protection from external influences, such as human intervention [3]. Microbial biofilms are ubiquitous and can be beneficial as well as detrimental to us [4].
Bacterial cells are often dispersed in a flowing fluid and colonize immersed surfaces [5]. For instance Neisseria gonorrhoeae has to resist the flow of urin, as it mostly affects the genitourinary system. Hence, studying bacterial adhesion under flow is of significant practical relevance. Therein, viscoelastic properties are an important aspect, as these are part of what makes bacterial aggregates resilient and hard to remove [6]. Insight toward which factors affect such properties may help in treatment of harmful bacterial infestation [7]. On the other hand, it may also aid in creating and maintaining similarly resilient, beneficial materials. Therefore it is not surprising that research regarding mechanics and viscoelasticity of biofilms has steadily grown in the past decades [6].
The same is also true for the field of active colloidal matter [8]. Independently moving and interacting bacteria suspended in fluids can be categorized as such. This is an important class of soft matter generally, because it shows emergence of unique mechanical and dynamic properties. Hence materials with embedded activity make possible applications in industrial coatings, medicine and robotics interesting [9].

To possibly aid in these endeavours, this thesis investigates rheologic properties of a network of active colloidal matter in the form of a bacterial colony. To this end, such a model is numerically implemented. It is a hybridised and modified version of previously proposed models for microcolonies of the Neisseria gonorrhoeae bacterium. The system is tested with dynamic mechanical analysis. Here controlled shear deformation in oscillating form is used. Several amplitude as well as frequency sweeps are executed. Thereby the viscoelastic moduli are determined in dependence of the amplitude and frequency of deformation, which describes the viscoelastic behaviour of a material to a large extent. Particular attention is given to the aspect of activity.

2 Background

2.1 Active colloidal matter

Active matter describes a collection of agents that autonomously use energy drawn from the environment for non-thermal work, mostly motion. Hence such systems are far from equilibrium [10]. There are many examples of active matter in nature. It ranges from swarm behaviour of animals like birds or fish on the scale of kilometers, down to coordination of molecular motors within cells on the nanometer scale. In between fall self propelled microorganisms, which include nematodes, algae, protozoa and bacteria [11]. As these mostly live in fluid environments, they fall in the category of colloidal matter. Studying active colloids is of scientific relevance, because they exhibit an array of extraordinary behaviour. Examples are clustering, phase separation, anomalous shear viscosities and giant density fluctuations [9] [10][11]. In practice, insight into such systems is of interest to possibly tackle the mechanisms behind harmful instances, such as bacterial pathogens. It may also help in the development of artificial swimmers like microrobots for drug delivery [8][12].

2.2 Neisseria gonorrhoeae

Neisseria gonorrhoeae (Ng) is a Gram-negative bacterium that is pathogenic to humans. It is the cause of gonorrhea, commonly known as the clap, which is the second most commonly sexually transmitted disease [13]. This mostly affects the genitourinary system and often goes unnoticed in women, which can lead to infertility [14].
The pathogenic mechanism involves attachment of the bacteria to epithelial cells via pili [15] (see next section) and the release of outer membrane fragments. Those fragments, called blebs, contain outer membrane proteins, lipopolysaccharides as well as DNA and RNA. The lipopolysaccharides act as an endotoxin to the human body [14]
Ng bacteria appear as diplococci, meaning that the singular cell bodies (cocci) are predominantly paired with flattened touchings sides.The resulting shape can be compared to that of a coffee bean. Sizes of the individual cells range around 0.6 to 1.0 μm [14][16].

2.3 Type IV pili and twitching

Ng is a bacterium that shows twitching motility. This is a form of bacterial movement across moist surfaces, which is irregular and presents itself in a jerky cell body translation.It is enabled by appendages on the bacterium called *type IV pili* (TFP) and therefore is flagella-independent. Twitching occurs as these TFP independently elongate, attach and retract, pulling the body with them. A common analogue is the use of a grappling hook [17]. However, as Ng cells usually have a number of pili in the order of 10 , this is rather a tug-of-war than a coordinated use of such. Thus arises the aforementioned style of movement [18][19].
TFP are means of rapid host colonization, adherence to host cells, bacteriophage adsorption, DNA uptake and formation of biofilms and microcolonies [2]. They have

been observed in a variety of bacteria, almost exclusively Gram-negative. Apart from Ng, the most studied examples are Pseudomonas aeruginosa and Myxococcus xanthus [17], which have been a source of recent discoveries [20][21], see section 2.6. TFP have a diameter of about 5 nm and their length is in the range of several micrometers. The process of pilus dynamics (elongation, attachment and retraction) stems from ATP-dependent association and dissociation of polymer subunits [22]. These polymers are called pilin proteins, or simply pilin. In a complex mechanism that is not yet fully understood, they are extruded from and collapsed into a reservoir in the inner cell membrane by a molecular motor protein complex [17]. However, it is known that this occurs at staggering rates of about 1000 sub-units per second [23].
Experiments using optical tweezers revealed that TFP mostly generate forces in a range below 100 pn , but it can also reach up to about 140 pn. This makes them the strongest known molecular motor and 30 times as strong as muscle myosin [24]. Through atomic force microscopes it was observed that TFP have elastic properties, as they elongate and get thinner when being pulled. This is probably caused by conformational plasticity of the pilin. Elasticity of TFP would be beneficial to bacteria in the colonization of host cell surfaces with high flow of bodily fluids [6][23].

2.4 Bacterial colonies

As a survival strategy on surfaces, most types of bacteria adhere to neighboring cells and thus create communities. This can protect them from displacement, environmental impacts or even human intervention, like antimicrobial treatment [3][6].
The most prominent example are biofilms. They occur on almost any moist surface with nutrients [7]. Structurally, biofilms are aggregates of bacteria embedded in an extracellular matrix of secreted biopolymers [25]. Although biofilms can be made use of, as in sewage treatment or waste processing, they predominantly enable bacteria related problems. Some examples of this are infections, tooth decay and fouling of industrial equipment [1] [26] [27] .
Another type of bacterial community are microcolonies. They often arise in the process of biofilm formation, but can also form outside of this context. These are agglomerates of dozens to thousands of bacterial cells. [28]. There are several methods through which bacteria can aggregate, one of them being TFP.
The production of the extracellular matrix in the transition from microcolony to biofilm may be enabled by a mechanism called *quorum sensing*, meaning the change in gene expression by bacteria through sensing local population density. Bacteria might thus become less motile and increase polymer secretion when they aggregate, such that a biofilm can be formed [29][30]. It has been observed that Ng forms microcolonies [31] as well as biofilms [13] [32].

2.5 Viscoelasticity

If no other source is given, the claims in this section can be found in [33].

2.5.1 Basic theory

Materials can be categorized according to their rheologic properties, meaning their behavior when deformed. One rheologic test is the response of a system to being sheared. Shearing an object is defined as deforming it parallel to one of its surface planes. The important measures are the shear stress σ and shear strain γ. The former is the quotient of the tangential force F acting on the object's plane with area A, as described by eq. (1). Corresponding displacement Δs of the plane parallel to the force, in units of the object's height h, produces the strain, see eq. (2).

$$\sigma = \frac{F}{A} \tag{1}$$

$$\gamma = \frac{\Delta s}{h} \tag{2}$$

There are two extremes in the way a material can react to deformation, namely elastic and viscous.

An **elastic** response is immediate and reversible. The energy causing deformation is conserved. Shear stress σ and strain γ have a time independent, direct relationship $\sigma = f(\gamma)$. In the linear case $\sigma = G_e\gamma$ the proportionality factor G_e is called the elastic module. An example material is a hard crystal, where the elastic forces stem from the displacement of molecules in their lattice potential well. Digression from linearity is called either *softening* or *stiffening*, depending on the elastic module becoming smaller or larger with strain.
For all physical materials there is a softening point, since particles are lifted out the well or elastic bonds of other sort are broken. This is called the *yield point* γ_L, after which the material is permanently deformed.

On the other hand, **viscous** materials respond in a rate dependent and dissipative manner to shear. Here stress is a function of the strain rate $\sigma = f(\dot{\gamma})$ and therefore indirectly time dependent, since $\dot{\gamma} = \frac{d}{dt}\gamma(t)$. Linear dependence $\sigma = \eta\dot{\gamma}$ is linked by the viscosity η. Viscous stress arises through frictional forces within the material and can therefore be observed in any particulate matter. Fluids with linear viscosity are called *Newtonian fluids*. Thus Non-Newtonian fluids encompass all nonlinear behaviour. Shear driven increase in viscosity is titled *thickening* and decrease *thinning*. Such nonlinearities may arise through processes like the breakage of bonds, emergence or loss of cross-links and entanglements.

Viscoelastic matter shows a combination of both of those extremes. There is an elastic and a viscous contribution in the response to being sheared. Most materials actually have some degree of viscoelasticity under appropriate circumstances. A commonly used example for viscoelastic materials are polymer chain networks. They

can have several types of inter-chain bonds contributing the elasticity, but chains can also detangle, stretch and move past each other without destroying the material [34].
In the linear approximation a viscoelastic response takes the form of eq. (3). This is called the *Kelvin-Voigt model*. A mechanic analogue is a spring and a damper coupled in series. Assuming the strain takes on a sinusoidal form of frequency f and amplitude γ_0, see eq. (4), the stress can be calculated as eq. (5). Here G' and G'' are the reformulated *viscoelastic moduli*, also referred to as *storage* and *loss modulus*.

$$\sigma = G_e\gamma + \eta\dot{\gamma} \tag{3}$$
$$\gamma(t) = \gamma_0 \sin(2\pi f t) \tag{4}$$
$$\sigma(t) = G'\gamma_0 \sin(2\pi f t) + G''\gamma_0 \cos(2\pi f t) \tag{5}$$

It follows that with moduli in the form of eqs. (6) and (7) the shear stress is also sinusoidal, shifted relative to the strain by a phase δ, see eq. (8).

$$G' = \frac{\sigma_0}{\gamma_0}\cos\delta \tag{6}$$
$$G'' = \frac{\sigma_0}{\gamma_0}\sin\delta \tag{7}$$
$$\sigma(t) = \sigma_0 \sin(2\pi f t + \delta) \tag{8}$$

The same result can be achieved by switching to the complex plane, where the physical values are represented in the real part. Again assuming an input of oscillating form as in eq. (9), the phase difference between elastic and viscous response is reflected in real and imaginary component. Thus the viscoelastic moduli can be combined in the *complex* or *dynamic modulus* G^*, as formulated in eq. (11).

$$\gamma^* = \gamma_0 e^{i\cdot 2\pi f t} \qquad \gamma = Re(\gamma^*) \tag{9}$$
$$\sigma^* = G^*\gamma^* \qquad \sigma = Re(\sigma^*) \tag{10}$$
$$G^* = G' + iG'' = \frac{\sigma_0}{\gamma_0}e^{i\delta} \tag{11}$$

The storage modulus G' is by definition equal to the elastic module G_e. Its name is based on the fact that it is proportional to the energy stored in the material through deformation. Similarly, the loss modulus G'' is proportional to the energy lost through dissipation. It is linked to the viscosity by $G'' = 2\pi f\eta$. Experimental implementation of a sinusoidal deformation is a common rheological test called *dynamic mechanical analysis* (DMA). Therein, either stress or strain are prescribed to oscillate harmonically, while the second variable is measured. With knowledge of input frequency, the amplitude of both measures and the phase difference between them, the viscoelastic moduli can be calculated. This can even be extended to not fully linear responses, as long as a definitive amplitude and phase lag can be determined [35].

2.5.2 Parameter sweeps

Rather than the values of the moduli themselves, most times their relative amplitudes in dependence of an adjustable parameter is investigated. Often these parameters are shear amplitude and frequency, but also temperature, solution concentrations and many others can be of interest. The course of the moduli provides an idea of the relative amounts of elastic energy and viscous dissipation in the material during flow [36]. This is achieved through sweeps, meaning incrementally increasing one parameter value, while all other remain constant.

First, the general aspects of *amplitude sweeps* are considered, where a range of strain amplitudes γ_0 is probed. At small values of γ_0 it is more likely that no structural reconfiguration has to occur and thus elastic bonds stay intact. Therefore the elastic contribution generally is at its maximum here. Linear elastic stress that is much larger than the present viscous contribution results in a plateau of G' and G''. This is called the *linear viscoelastic region* (LVER). Tests with harmonic deformation inside of this region are called *small amplitude oscillatory shear* (SAOS). When the elastic component is larger than the viscous, the material is regarded *solid-like*.
At the aforementioned yield point the initial configuration begins to be irreversibly broken and flow occurs. As the elastic contribution to the stress decreases, viscous effects become more prevalent. When the viscous component G'' is larger than the elastic G', the material is in a *liquid regime*. In practice this does not occur at a definitive strain amplitude, but rather over an extended region called the *solid-liquid transition*. For many viscoelastic materials, slow flow at the beginning of this transition enables the network of interactions to reform after plastic deformation. This ceases to be true at higher flow, caused by larger shear amplitudes [36]. Then also hydrodynamic effects come into play, such as alignment, entanglement and flow channels [37]. Also *wall slip* can occur, which is a discontinuity of the velocity profile at the sheared plane due to missing interaction between the bulk material and the wall [36].
Hyun *et al.* [37] identified four archetypes of viscoelastic behaviour for *large amplitude oscillatory shear* (LAOS), namely Strain thinning, strain hardening, and weak and strong strain overshoot. Their characteristic shape is depicted in fig. 5 from [37]. For the process of this conclusion and the mechanism behind each type please refer to the source [37], as this is too extensive to be presented here.
In a *frequency sweep* the shear amplitude is maintained while the frequency increases. An ideal linear viscoelastic material has a constant elastic contribution to shear stress, while the viscous component increases proportionally with frequency. However physical systems have certain response or relaxation times, leading to frequency dependent elasticity. A common result of a frequency sweep for simple viscoelastic models shows an increase of both G' and G'' with frequency, with the ratio $G''/G' = \tan\delta$ becoming larger as viscous effects dominate [34] [38]. Thus frequency sweeps are generally executed within the LVER, otherwise elastic effects may be overshadowed. The actual course of G' and G'' over frequency varies strongly between materials, as it is highly dependent on the internal time scales of the processes that cause the elastic and viscous stresses.

2.5.3 Exemplary results

As it is referenced multiple times, relevant aspects of Townsend and Wilsons findings regarding a bead-spring dumbbell solution are briefly presented [39].
The model consists of spheres suspended in a Newtonian fluid, which are coupled pairwise by a spring with a natural length L. We are only interested in the case of Hookean linearity with spring constant k, but they also investigate other dependencies. The spheres are modeled in three dimensions, but are confined to a single layer, therefore being effectively two dimensional.
They use DMA to determine the viscoelastic moduli G' and G''. Varying values of L, k as well as the area concentration of beads c are simulated.
Results in amplitude sweeps of this model are all similar to the generic example can bee seen in fig. 6 from [39]. It shows strain thinning in the viscous component and an overshoot in the elastic one for LAOS. Thus it is a hybrid between type I and type IV with respect to the LAOS types according to Hyun *et al.* [37]. Increasing spring constant k leads to the maximum in G' becoming more pronounced.
SAOS frequency sweeps also have a characteristic course in G' and G'', regardless of choice of parameters. This is illustrated in fig. 3 from [39]. For varying values of k the curve is only slightly shifted and distorted. Changing L and c has similar effects.
Both moduli initially increase with frequency. Then G'' assumes a global maximum and decreases subsequently, whereas G' begins plateauing. The intersection of G' and G'' is seemingly incidental with the maximum of the latter, regardless of parameter choice.
They identified the intersection to be at a frequency that corresponds to the dumbbells relaxation time $\tau_r = 1/\omega(G' = G'')$.

2.6 Current research

For of similar types of bacteria like Ng, meaning such that use TFP, there were several recent discoveries in their dynamic behaviour.
It was observed experimentally, that wild type Pseudomonas aeruginosa outcompetes a hyperpilated mutant at high cell densities. Using liquid crystal theory, it is revealed that faster bacteria cause topological defects in the cell alignment to collide, trapping cells in place. Thereby it is shown, that slow motion is key to bacteria moving in vast, dense collectives. [21] .
Such topological defects also are of importance for Myxococcus xanthus. Defects with a single axis of symmetry are found to generally promote the formation of cell layers and thus seeding fruiting bodies. However, defects with three symmetry axis preferentially cause holes in the collective to open. Is is suggested that cell motility and mechanical cell–cell interactions are sufficient to produce this effect [20].

Also, combining Computational Fluid Dynamics with a Discrete Element Method, a model for rod shaped bacteria with TFP was found, which successfully predicts their upstream twitching motility in shear flows. Thus other phenomena this model suggests, like an optimal wall shear stress for upstream twitching or accumulation on groove surfaces, might also be accurate. [40]
Regarding active colloids, it was observed that autonomous dynamics of embedded active colloids decrease the elasticity of fractal cluster gels. Contrary to that, myosin motors show stiffening effects when added to gel networks [9].

This shows that there is substantial interest in areas touched in this thesis and much to be learned about and from such systems. This thesis is an attempt to contribute in that respect.

3 Methods

3.1 Ng colony model

In the simulations colonies of Ng cells are modeled with *Stokesian Dynamics* in a two dimensional box. The box has width B_x and height B_y. There are periodic boundary conditions in the first dimension. Duration of a single simulation is denoted with $\mathcal{T}$ and the number of cells with N_{cell}. These may vary for some simulations and are given explicitly in that context if so. Their default values for the main simulations and all other model parameters are given in table 1. It has to be noted that the units of all calculations do not have direct physical validity, since they result from simulations of a deeply simplified model with unvalidated parameters.

3.1.1 Cell and pili dynamics

The cells are simplified to having rigid circular bodies. Their radii r_i follow a normal distribution with mean $\overline{r_{cell}} = 0.5\,\mu$m and variance root $\frac{\overline{r_{cell}}}{10}$. When cells overlap they exert a repulsive force, see section 3.1.2.
Cell movement is governed by a *Langevin-equation* (12) without stochastic forces. Here x_i is the position of the i-th cell, μ the effective friction coefficient and F_i the total force acting on cell i. Time integration is done with the Euler method with time step δt, eq. (13). Since the modeled cells are practically symmetric to rotation, torque is not regarded in this model, as it should not have significant impact.

$$\dot{x}_i = \mu \cdot F_i \tag{12}$$

$$\delta x_i = \mu \cdot F_i \cdot \delta t \tag{13}$$

Each cell carries N_{pil} pili. They are modeled as straight lines, described as vectors with their origin on the cell surface. Thus, the surface is split up into N_{pil} equal sections in each of which a pilus anchor is placed randomly. From those, pili grow and retract to with a velocity of v_{pil}, meaning their length L_{ij} (cell i, pilus j) increases according to Euler method integration. There is no volume exclusion between cell bodies and pili.
At the start of a growing phase, the direction of growth is chosen randomly in a θ_{pil} angle from the orthogonal to the surface tangent. When a pilus grows up to a certain length it stalls. This length threshold is drawn from an exponential distribution with mean L_{max}. A stalling pilus attaches to the substrate with probability p_{subs}. If it does so successfully, it begins pulling the cell body toward its tip. The position of the pilus tip remains constant, as long as it is attached to the substrate. If the attachment process fails the pilus retracts. Then, when its length is below a value of L_{min}, the growing phase is initiated. At the start of every growing phase the maximum length and the growth direction are generated anew.
During its growth a pilus can attach to pili of other cells. This occurs with a probability of p_{pil} when its tip is within an extended area around the other, as pili are volatile in practice [27]. The area is defined as an isosceles triangle with its apex lying at the anchor and the pilus vector being the height. The base, with its center

at the tip of the pilus, is b_{pp} times the pilus length L_{ij}. Therefore the maximal orthogonal distance from tip to pilus increases linearly with distance from the anchor. This is illustrated in fig. 1(a). When two pili attach to one another, they align along the straight connecting their anchors with touching tips. The ratio of their lengths before attachment is conserved after.

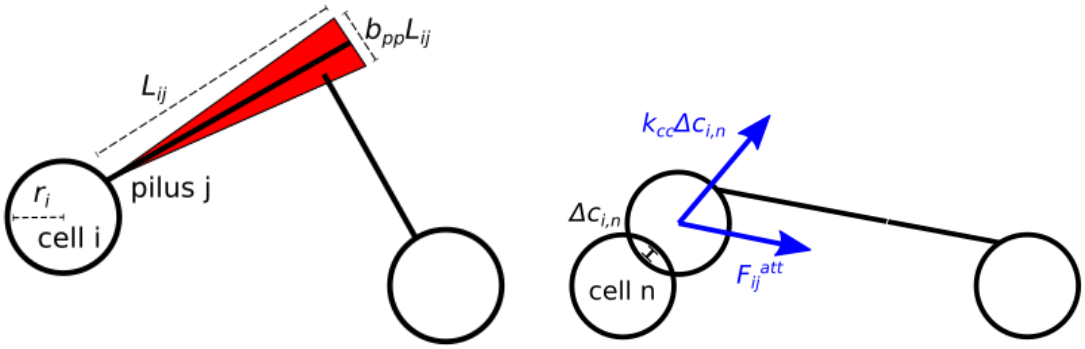

(a) Pilus-Pilus attachment process (b) Force diagram

Figure 1: Illustration of attachment process between two pili. a) Before attachment the tip of one pilus must lie within the isoceles triangle around the other, dimensions given in picture. b) Forces acting on cell i, resulting from pilus-pilus interaction and cell-volume exclusion.

While a pilus is attached to the substrate or another pilus and pulls and shortens monotonously, it exerts a constant force F_p onto the cell body. If it is lengthened during attachment due to other acting forces, the pulling force increases. The pilus then acts as a spring with a spring constant k_{pil}, see eq. (14). The symbol Θ represents the Heaviside function, which takes value 1 for arguments above 0 and is 0 otherwise. The extension ΔL_{ij} is given as the difference between the current length and the minimum length L_{ij}^{min} of the pilus during the current pulling phase , see eq. (15) (t_0 marks start of phase).

$$F_{ij}^{att} = F_p + k_{pil}\Delta L_{ij} \cdot \Theta\left(\Delta L_{ij}\right) \tag{14}$$

$$\Delta L_{ij}(t) = L_{ij} - \min\left(\{L_{ij}(t') \right\} \quad | \quad t \in [t_0, t]) \tag{15}$$

There are several processes that trigger detachment of a pilus in the pulling phase. If a pilus detaches in such a way or simply does not attach when stalling, it begins retracting.

- The length of the pilus falls below L_{min}.
- The pulling force exceeds a threshold F_{th}.
- A predetermined maximum duration of attachment is exceeded. This duration is drawn from an exponential distribution with mean T_{hold} at the start of the pulling phase.

- If two pili are attached to each other, detachment of one, through any above reasons, causes both to retract.
- Pili can also attach to others, that currently are in their pulling phase. Successful attachment causes the bond to reform. If the previously pulling pilus was attached to a third pilus, the latter detaches.

3.1.2 Forces

The total force F_i on a cell is the sum of all acting forces from pili F_{pil} and cell-volume exclusion F_{cc}. This is formulated in eq. (16) and illustrated in fig. 1(b).
In the cell-volume exclusion, eq. (17), the involved symbols are the effective spring constant k_{cc}, the amount of cell overlap $\Delta c_{i,n}$ and the normalized connection vector between the cell centers $\widehat{\Delta x_{i,n}}$ for cell i when overlapping with cell n. The sum is over all possible cell pairs, but the Θ only makes those with positive overlap count.
In the term regarding the force from pili, eq. (19), the Heaviside functions symbolise the state of attachment. Θ_{ij}^{att} takes value 1 as soon as the pilus attaches and 0 after it detaches. The two other Θ's represent the detachment. They become 0 when the pilus force exceeds the threshold F_{th} or the pulling phase exceeds the maximum duration T_{ij}^{hold}, generated at start of the pulling phase t_0. The value of pili contribution F_{ij}^{att} is described above, see eq. (14).

$$F_i = F_i^{cc} + F_i^{pil} \tag{16}$$

$$F_i^{cc} = \sum_{n=0}^{N_{cell}} k_{cc} \Delta c_{i,n} \cdot \widehat{\Delta x_{i,n}} \Theta\left(\Delta c_{i,n}\right) \tag{17}$$

$$\Delta c_{i,n} = \left((r_i + r_n) - \|\Delta x_{i,n}\|\right) \tag{18}$$

$$F_i^{pil} = \sum_{j=0}^{N_{pil}} F_{ij}^{att} \cdot \Theta_{ij}^{Att} \Theta\left(F_{th} - F_{ij}^{att}\right) \Theta\left(T_{ij}^{hold}(t_0) - (t - t_0)\right) \tag{19}$$

3.1.3 Shear

The viscoelastic properties of a microcolony will be investigated. Thus the cells in the box have to be subjected to shearing.
Here *controlled shear deformation* is implemented, meaning that the strain is prescribed and the stress response recorded. It is carried out through adding rows of cells as walls, simulating a flowing layer. Specifically, N_{wall} cells are fixed with their center at the upper and lower border of the box, respectively. They are spaced equidistantly along the width B_y. These cells do not move according to the force acting onto them, but rather laterally with a prescribed velocity v_{wall}, see eq. (20). Lower and upper wall move in opposite directions.

$$\delta x_{up}(t) = -\delta x_{low}(t) = v_{wall}(t)\delta t \tag{20}$$

A practical setup that resembles this symmetry is the *Couette-Taylor-Flow*. Here the probed material is enclosed between two rotating cylinders.

For DMA, the system is simulated under sinusoidal strain, see eq. (4). It is applied with given a frequency f and strain amplitude γ_0. Thus the wall cells have to move according to eq. (21), with the prefactor arising through differentiation and using eq. (2) for two walls that are B_y apart.

$$v_{wall}(t) = \gamma_0 \frac{B_y}{2} \cdot 2\pi f \sin(2\pi f t) \begin{pmatrix} 1 \\ 0 \end{pmatrix} \tag{21}$$

Table 1: Model parameter values and definitions

parameter	value	definition	reference
B_x	$28\,\mu$m	box width (+ periodic boundaries)	
B_y	$7\,\mu$m	box height	
N_{cell}	120	number of cells in colony	
N_{wall}	20	number of wall cells per wall	
$\mathcal{T}$	500 s	duration of simulation	
δt	0.001 s	time step for Euler time integration	
μ	$14\,\frac{\mu\text{m}}{\text{nN}}$	translation mobility	[41]
p_{subs}	50 %	attachment probability to substrate	[41]
p_{pil}	90 %	attachment probability to other pili	
b_{pp}	$\frac{1}{5}$	base to height ratio for pili attachment range	
v_{pil}	$2\,\frac{\mu\text{m}}{\text{s}}$	pilus growth and free retraction speed	[41]
T_{hold}	50 s	mean of pilus detachment time distribution	[27]
L_{max}	$2\,\mu$m	mean of maximum pilus length distribution	[41]
L_{min}	$0.1\,\mu$m	threshold for fully retracted pilus	
F_p	0.1 nN	constant pilus pulling force	[41]
k_{cc}	$20\,\frac{\text{nN}}{\mu\text{m}}$	spring constant cell-cell volume exclusion	[27]
k_{pil}	$2\,\frac{\text{nN}}{\mu\text{m}}$	spring constant of stretched pili	[27]
F_{th}	0.14 nN	force threshold for pilus detachment	[24]

3.2 Simulation procedure

Here the process of simulation for the following sections and its preparation are briefly summarized.
When subjecting a system to external perturbation, here being sheared, it should initially be in a steady state. Therefore a transient simulation is run for $\mathcal{T} = 1000s$ with random initial conditions (see below) and no shear. This duration is significantly larger than any conceivable time scale of internal dynamics. Thus transient effects from an artificial initial state are eliminated and the network reaches a dynamic steady state. The final state of this simulation is then taken as the initial condition for all following simulations.
With this, then the network is simulated for $\mathcal{T} = 3000\,\mathrm{s}$, again without external influence. Being equlibrated from the start, the system is in a dynamic steady state over the entire duration. Analysis of the occurring cell movement can thus be used to evaluate characteristic measures of internal dynamics.

Finally, the periodically sheared system can be simulated. Amplitude sweeps are executed for constant frequencies of $f \in \{0.04\,\mathrm{s}, 0.125\,\mathrm{s}, 0.04\,\mathrm{s}\}$ and frequency sweeps at strain amplitudes $\gamma_0 \in \{0.05, 0.1, 0.2\}$, respectively. These values, as well as the range within the sweeps, were chosen due to preliminary simulations that gave insight into the approximate parameter choice of feasible data.
The run time for these simulations is $\mathcal{T} = 500\,\mathrm{s}$ and the data is saved in intervals of $0.1\,\mathrm{s}$. At large frequencies this was modified to get at least 25 data points per period.

In the following it is briefly explained what is referred to as random initial conditions. The cell positions are uniformly distributed inside the box, without regard to overlap of the cell bodies. Since the pili of a cell are indexed clockwise, the first pilus' anchor is given a random offset between 0 and 2π, such that looping through indices does not produce systematic errors. All pili variables that have to be repeatedly generated anew (maximum length, growth direction, maximum attachment duration) are drawn from those distributions. The status of all pili is set to growing. Since the pili dynamics are significantly faster than those of the cells, this does not have long lasting consequences.

3.3 Analysis

3.3.1 Mean squared displacement

The *mean square displacement* (MSD) is a measure of diffusion for systems with random motion. There are several definitions of it, encapsulating similar concepts. Here the definition given in eq. (22) is used, where the displacement is taken as the absolute difference of the cell position at time t with respect to its initial state. It relates to the diffusion coefficiant via eq. (23). n is the degrees of freedom for cell translation, here 2. The MSD follows a power law dependence over time. Regular diffusion results in a linear increase. An exponent smaller than 1 characterizes subdiffusion, superdiffusion if larger.

$$MSD = \frac{1}{N}\sum^{N}\|x_i(t) - x_i(0)\|^2 \tag{22}$$

$$MSD = 2nDt \tag{23}$$

$$\tag{24}$$

3.3.2 Overlap correlation function

To determine time scales of dynamics in the bacterial system, a two-point density correlation function ξ is implemented, analogous to *overlap correlation functions* (OCF) used in glassy liquid analysis [42]. It is dependent on a distance threshold parameter d and and a start time t_0. The weight function $w(d, \Delta x_{i,j})$ produces 1, if the distance between two cell centers $\Delta x_{i,j}$ is smaller than d and 0 otherwise. Summing over the dynamic set $\mathcal{S}_i(t)$ enacts that the weight function is only evaluated for cells that are within the distance threshold since the start time t_0.

$$\xi(d, t_0, t) = \frac{1}{w_0}\sum_{i=0}^{N_{cell}}\sum^{j\in\mathcal{S}_i(t)} w\left(d, \Delta x_{i,j}(t)\right) \tag{25}$$

$$\mathcal{S}_\rangle(t_0, t) = i \in \mathbb{N},\, i < N_{cell} \,|\, w\left(d, \Delta x_{i,j}(t')\right) = 1\, \forall t_0 \leq t' < t \tag{26}$$

$$w\left(d, \Delta x_{i,j}(t)\right) = \Theta\left(\|x_i(t) - x_j(t)\| - d\right) \tag{27}$$

$$\xi(d, t_0, \tau) = \frac{1}{e}\xi(d, t_0, t_0) \tag{28}$$

Simply by its definition, $\xi(t)$ is a monotonously declining function. In a diffusive system it follows an exponential decline. The time τ at which it reaches $1/e$ of its value at t_0 is a measure of diffusion with respect to the length scale d. It measures the characteristic time after which cells that are within a radius of d at time t_0 have moved out of that circle.

3.3.3 Shear measures

Although the strain $\gamma(t)$ follows a prescribed pattern, for the analysis it is determined from the wall cell movement to forgo systematic errors. To this end absolute cell positions X, that disregard the periodic boundary conditions, are used. For each wall an example cell is chosen. Which does not matter, as they move synchronously. Its displacement from the center position $X - \overline{X}$ is analogous to the displacement Δs in eq. (2). Since the walls move in opposite directions, the difference between lower Δs_{low} and upper wall displacement Δs_{up} in relation to the box height constitutes the strain, see eq. (29).
To calculate the corresponding stress $\sigma(t)$, the force acting on the walls in direction of the displacement needs to be known. For each wall it is given as the sum of the negative of the total forces on the wall cells $F_{i_{low/up}}$ in x-direction, as these have to be overcome by the cause of shear deformation. Here $i_{low/up}$ is in reference of the set of N_{wall} cells fixed at lower and upper border, respectively. Again the difference has to be considered, see eq. (30).

$$\Delta s(t) = \Delta s_{low} - \Delta s_{up} = \left(X_{low}(t) - \overline{X}_{low}\right) - \left(X_{up}(t) - \overline{X}_{up}\right) \tag{29}$$

$$F(t) = \sum_{i=0}^{N_{wall}} F_{i_{up}}(t) - \sum_{i=0}^{N_{wall}} F_{i_{low}}(t) \tag{30}$$

$$h = L_y \qquad A = L_x \tag{31}$$

The dynamic moduli G' and G'', as defined in equation (6) and (7), require knowledge of stress amplitude σ_0 and phase lag δ. This can be done under the presumption that the force is sinusoidal. However, because there are strong fluctuations in the data obtained through eq. (30), it is first averaged over its period. This means that for each saved time t_n within the period T, the arithmetic mean of all N values of the force F at times that differ by a multiple of the period is taken, see eq. (32).
Then the *optimize.curve_fit* algorithm from the *Python SciPy* library is used to fit a sine function of the form (33) to the resulting data. It uses nonlinear least squares technique with regard to second and third parameter, since the frequency is fixed. Errors of the input data are used as absolute weights. Then σ_0 and δ result through eqs. (38) and (35). Having $\phi = 0$ means in phase with the strain.

$$< F(t_n) >_T = \frac{1}{N+1} \sum_{n=0}^{N} F(t_n + nT) \tag{32}$$

$$f(t, F_0, \phi, f) = F_0 \cdot \sin\left(2\pi f t + \phi\pi\right) \tag{33}$$

$$\sigma_0 = \frac{F_0}{B_x} \tag{34}$$

$$\delta = \phi\pi \tag{35}$$

$$\tag{36}$$

3.3.4 Errors

For all calculated variables g, their errors Δg are determined with the standard error propagation formula eq. (37). The function depends on n variables a_i with respective errors Δa_i.

$$\Delta g(a) = \sqrt{\sum_{i=1}^{n} \left(\frac{\partial g}{\partial a_i} \Delta a_i \right)^2} \tag{37}$$

In the calculation of the viscoelastic moduli, eqs. (6) and (7), this yields eqs. (40) and (41). The errors stem from the fit parameters F_0 and ϕ, which first have to be converted to errors of σ_0 and δ.

$$\Delta\sigma_0 = \frac{\Delta F_0}{F_0}\sigma_0 \tag{38}$$

$$\Delta\delta = \frac{\Delta\phi_0}{\phi}\delta \tag{39}$$

$$\Delta G' = \sqrt{\left(\frac{\Delta\sigma_0}{\sigma_0} G' \right)^2 + (\Delta\delta \cdot G'')^2} \tag{40}$$

$$\Delta G'' = \sqrt{\left(\frac{\Delta\sigma_0}{\sigma_0} G'' \right)^2 + (\Delta\delta \cdot G')^2} \tag{41}$$

4 Results

In this section all results from simulations in the extent of this thesis are discussed. The findings are concluded at the end and a summary and outlook can be found in the the subsequent sections.

4.1 Model validity

Although the implemented model for a microcolony of Ng cells is contrived by slightly modifying a combination of models that were previously used, it will be shown that it carries validity. This is done by reproducing some important experimental observations for Ng at least qualitatively.

Firstly, the typical path of a cell showing twitching motility is looked at. The reference track of a Ng cell can be seen in fig. 1 from [19].
A single cell is simulated and the travelled path illustrated for the same timestamps as in the reference, see fig. 2. The extent of the box is made much larger than the travelled distance, such that it does not interfere.
Simulated and experimental path have a high resemblance. The movement is irregular and similar to Brownian motion. Also the extent of both paths is in the same order of magnitude. It should to be noted that this is achieved without directly applying a random force to the cell, but rather purely through the activity of multiple pili.

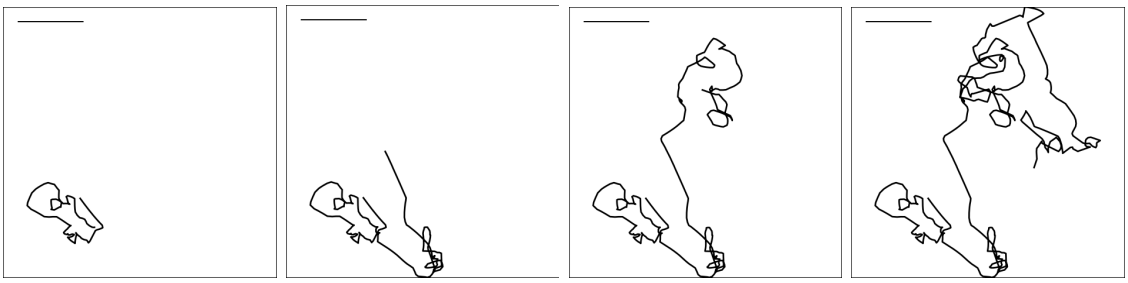

(a) 20 s (b) 40 s (c) 60 s (d) 100 s

Figure 2: Reproduction of twitching motion for a simulated cell at different times, bar represents 5 μm

Secondly, the clustering properties of Ng are tested. Taktikos *et. al* [31] investigated this experimentally and saw an approximate exponential decline with a y-offset in the temporal development of the number of aggregates (Fig. 2 in [31]).
To reproduce this, we simulate 600 cells inside a box of 60 μm height and width with periodic boundary conditions in both directions. The initial conditions are the same as for the transient simulation and the simulation time is $\mathcal{T} = 1800\,\mathrm{s} = 30\,\mathrm{min}$.
Initial and final states of cell bodies are depicted in fig. 3(a) and 3(b). From the uniform distribution at the beginning, the network transitions to a clearly clustered state.
An automated cluster counting method is implemented to quantify this. It counts

continuous chains of cells that are linked through pili attachment. The thus determined course of aggregates over time is illustrated in fig. 3(c). Single cells or subclusters frequently detach for short periods within a larger cluster. Since this method counts them separately, the actual number of clusters can be interpreted as the lower bound of the bulk scattered data points.
Although the system is much smaller than the experimental reference, the number of aggregates qualitatively behave very similar. Up to about 15 min the values decrease exponentially. After that point the graph remains constant on average. The mean number of aggregates in this region is 8 with a standard deviation of 3. This coincides with the earlier explanation and the 5 clusters visible during that time, such as in fig 3(b).
There is some disparity to the experimental reference [31] in the initial stages, but it may be explained by the bacteria in the experiment initially not being completely decoupled.

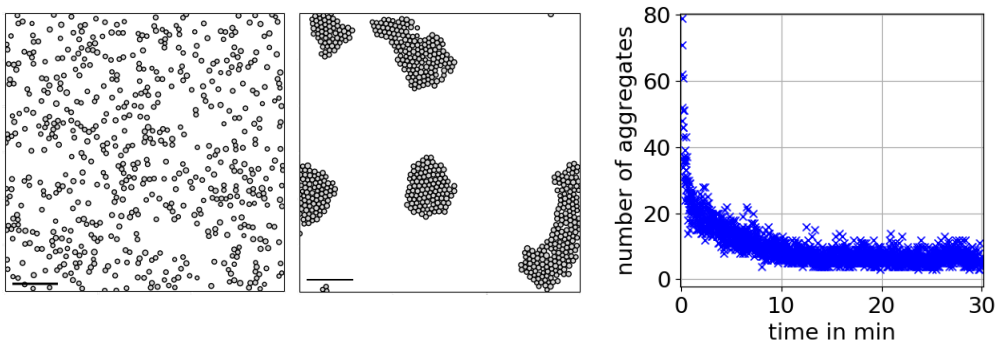

(a) Snapshot at 0 min (b) Snapshot at 30 min (c) cluster number over time

Figure 3: Clustering of model cells. Graphs a) and b) show snapshots of the system, without the pili of the cells being shown. Initial, randomly distributed state in a) and clustered state after 30 min in b). The bar represent 10 μm. c) Temporal development the number of aggregates, determined as uninterrupted pili-linked chains.

4.2 Steady state

At first the system without shear is investigated to analyse the networks steady state with regard to dynamic measures.
The initial state of this and all following simulations is illustrated in fig. 4. It is percolated in y-direction over a large fraction of the box width. Cell bodies are predominantly tightly packed. Pili lengths in the bulk are mostly in the order of magnitude of the cell radius. A large hole in the network shows the internal tension of the network, as the borders are concave. Therein extended pili can be seen.

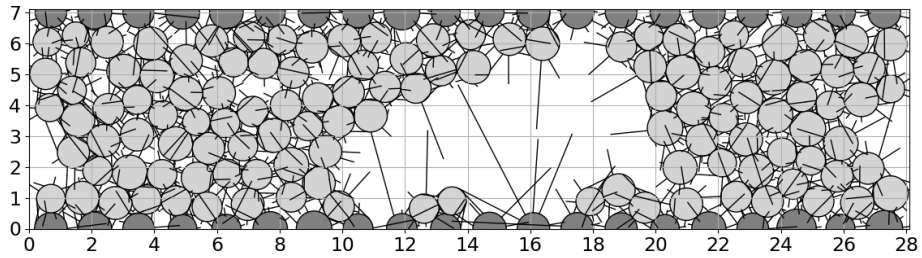

Figure 4: Initial state of network for all following simulations. Box dimensions are $B_x = 28\mu$m and $B_y = 7\mu$m.There are $N_{cell} = 120$ cells in the colony (light grey) and $N_{wall} = 20$ wall cells per y-border (dark grey).

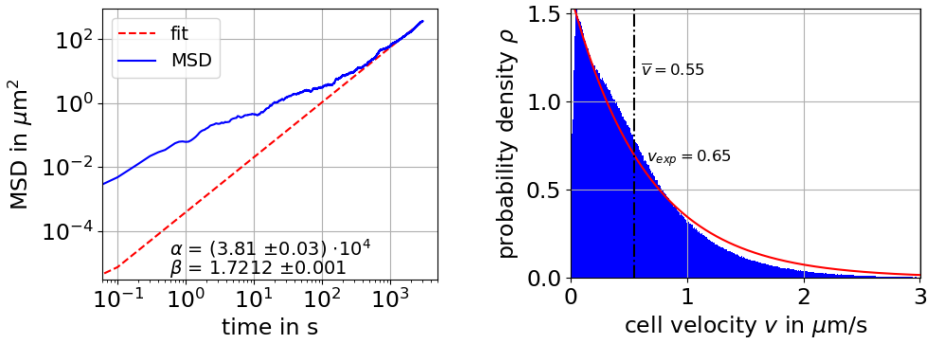

(a) MSD

(b) Cell velocity histogram

Figure 5: a) Time development of the MSD for the steady state with mononomial fit, parameters given in graph. b) Histogram of cell velocities. Mean velocity illustrated as a dashed line. The red line illustrates an exponential fit with scale parameter v_{exp}.

In fig. 5(a) the graph of MSD over time is depicted, as determined via eq. (22) for absolute cell positions X. A mononomial of the form αt^β is fitted to the curve. The resulting time exponent $\beta \approx 1.7$ classifies the system as having superdiffusion. Using eq. (23), the diffusion coefficient would therefore be time dependent $D \propto t^{\alpha-1}$. However, this is most likely affected by the non-isotropic geometry of the box and not purely representative of the internal dynamics. Therefore other measures of internal dynamics are investigated.

Table 2: Correlation time τ for various distance thresholds d in the OCF

d in μm	1.25	1.5	2	2.5	3	3.5	4
τ in s	8	21	33	47	66	88	119
std(τ) in s	2	6	7	11	14	18	21

The distribution of velocities of the cells might be of interest. A histogram of the cell velocities can be seen in fig. 5(b). Above a maximum close to 0, the velocities approximately follow an exponential distribution. Hence it is fitted with a curve of such a form $Ae^{-v/v_{exp}}$. The characteristic velocity v_{exp} of this curve, as well as the mean $\overline{v}$ are also given in the graph.

A third measure that is evaluated is the OCF, as defined in eq. (25). It is calculated for several different length thresholds d. The values are chosen larger than $d = 1\,\mu$m, since this is the average distance of touching cells. Again, the cell positions without periodic boundaries X are used. For a each value of d, the function is calculated for start times t_0 every 50 seconds in the simulation time $\mathcal{T}$. The resulting mean value of τ with regard to d and its standard deviation are listed in table 2.

4.3 Dynamic mechanical analysis

Now the network under shear is investigated. Before the analysis of the viscoelastic moduli takes place, the process of data analysis is discussed and shown exemplarily. The examples are taken from an amplitude sweep at frequency $f = 0.125\,\mathrm{Hz}$.
At first we look at a strain amplitude of $\gamma_0 = 0.1$. Fig. 6 displays the unmodified data of the x-component of force acting on wall cells for lower F_{low} and upper border F_{up}. It can be seen that the force fluctuates significantly and the underlying sinusoidal wave form is only barely visible. On the second y-axis the displacement of each wall Δs_{low}, Δs_{up} is plotted. The waves are shifted with respect to each other.

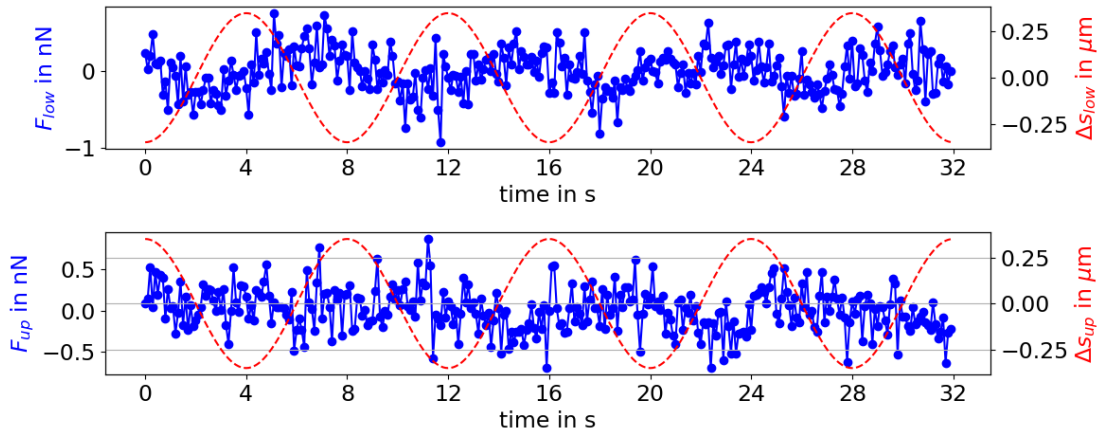

Figure 6: X-component of total force acting on wall cells $F_{low/up}$ and displacement of exemplary wall cells $\Delta s_{low/up}$ over time for the three periods of

Therefore the averaging over periods is performed, as described by eq. (32). The result is depicted in fig. 7(a). Here the assumption of a sinusoidal shape is valid and a function of the form (33) is fitted to the data. The resulting parameters are given in the graph.
In a *Lissajous-Bowditch* plot in fig. 7(b), stress is shown as a function of strain, removing time dependence. Errors stem from the standard error of period-averaging the force. It follows a normal distribution in the steady state, thus using the standard error is valid. The apparent shape of an ellipses is the regular outcome for two variables taking sinusoidal form with a phase shift between them. Irregularities from the ideal ellipses of the fit are encapsulated by the errors.

This example is well behaved, as the period averaged force shows a pronounced sinusoidal shape. However, for strain amplitudes at the edges of the sweep this is less valid. The graphs of period averaged force and fitted sine curve for those cases are depicted fig. 8.
For $\gamma_0 = 0.01$ the data is extremely noisy, see fig. 8(a). This is likely explained by the fluctuations through internal dynamics on this time scale overshadowing the response to such a small deformation. The fit errors, especially for the phase lag δ, are in the order of the values. It is attempted to get some statistical validity by running the same simulation several times and using averages in the calculation of

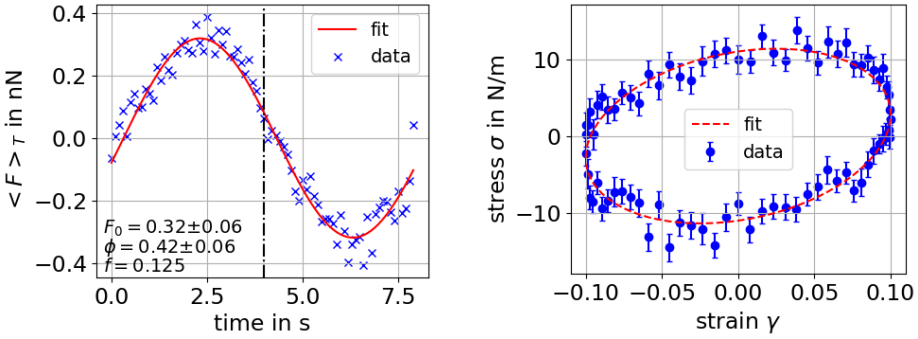

(a) (b)

Figure 7: a) Period-averaged wall force $< F >_T$ and b) Lissajous-Bowditch plot of stress and strain for shear at frequency $f = 0.125\,\mathrm{Hz}$ and strain amplitude $\gamma_0 = 0.1$.

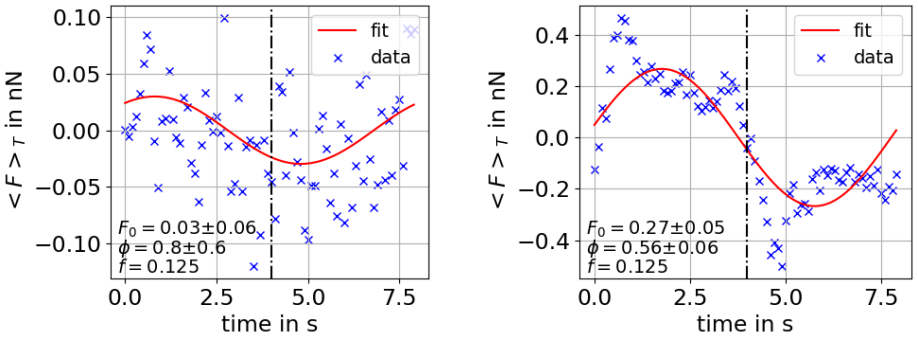

(a) $\gamma_0 = 0.01$ (b) $\gamma_0 = 1$

Figure 8: Examples of edge cases in the response to shear, for period-averaged force $\langle F_T \rangle$ for shear at frequency $f = 0.125\,\mathrm{Hz}$ and strain amplitude given below graph.

G' and G''.
On the other end of the swept range, at $\gamma = 1$, the wall force shows a clear response to the strain, see fig. 8(b). Yet now the assumption of linearity is invalid. Just after the minimum strain there is a pronounced onset peak. This leads into a local minimum at the maximal slope of the strain. Just before the strain maximum there is another small peak in the force. After that the mirrored course begins. The reason for this behaviour is probably based therein, that large strain rates cause cells to detach from the wall, but the activity enables them to reattach when the wall cells slow down. This can be seen in fig. 9. For the other amplitudes, the number of cells attached to the wall remains practically constant over the period. At the larger strain amplitude a significant number of cells detach from the wall, seemingly proportional to the absolute value of the strain rate $|\dot{\gamma}|$.

The sinusoidal fit in in fig. 8(b) does not encompass the shape of this nonlinear force response. For such data the phase difference is calculated manually. This is done by locating the onset peak and taking the time difference Δt_δ to the maximum of the strain. It is then converted into a phase with $\delta = 2\pi f \Delta t_\delta$. For instance in the case

depicted in fig. 8(b) this yields $\delta = 2\pi \cdot 0.125\,\mathrm{Hz} \cdot (3.3 \pm 0.2)\,\mathrm{s} = (0.825 \pm 0.05)\pi$. In the following such cases are illustrated with hollow instead of solid data markers. The amplitude of the fit will still be used, as it approximates the total magnitude of stress response.

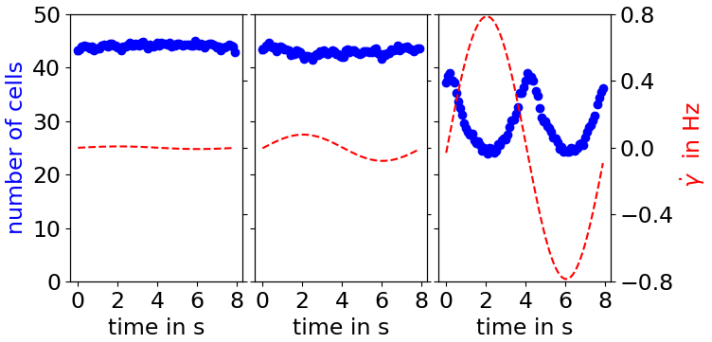

Figure 9: Number of cells attached to walls and strain rate for strain with $f = 0.125\,\mathrm{Hz}$ and (left) $\gamma_0 = 0.01$, (middle) $\gamma_0 = 0.1$, (right) $\gamma_0 = 1$.

With knowledge of stress σ_0 and phase shift δ, eqs. (6) and (7) can be used to calculate the viscoelastic moduli. One only has to convert the fit parameters F_0 and ϕ via eqs. (34) and (35). In this way the storage G' and loss modulus, G'' are evaluated for every simulated tuple of frequency and strain amplitude (γ_0, f) within the amplitude and frequency sweeps. Their errors result through eqs. (40) and (41).

4.3.1 Amplitude sweeps

Amplitude sweeps are performed in the range of $\gamma_0 \in [0.01, 1]$. The resulting stress amplitude σ_0 and phase difference δ of an amplitude sweep at frequency $f = 0.125\,\mathrm{Hz}$ is depicted in fig. 10(a).
Below strain of $\gamma_0 = 0.05$ both variables have errors in the order of magnitude of the values. An explanation for this is given in the previous section in reference to fig. 8(a). There is an increase of the stress amplitude up to about $\gamma_0 = 0.2$, while the phase difference remains approximately constant. This is in line with the expected behaviour of a viscoelastic material in the LVER. Then these the roles are reversed, with σ_0 plateauing and δ increasing. At even larger strains σ_0 decreases again, taking its maximum at $\gamma_0 = 0.3$. From this point on the response becomes nonlinear and the manually determined phase lags are used.
Within the assumption of a linear viscoelastic response, the phase lag can only take values of $\delta \leq \pi/2$. However, here the nonlinear phase calculation yields values approaching π. The limit case $\delta \to \pi$ would take the form of a Dirac-delta shaped peak in stress, in positive as well as negative direction, at the extremes of strain. Also, at small strain the heavily uncertain values of δ are also above $\pi/2$. Thus only within the region of about $\gamma_0 \in [0.02, 0.3]$ evaluation of the dynamic modulus via eq. (6), (7) has validity. It is still evaluated for every strain amplitude simulated. The graph of storage G' and loss modulus G'' over strain amplitude can be seen in fig. 10(b) in a double logarithmic plot.

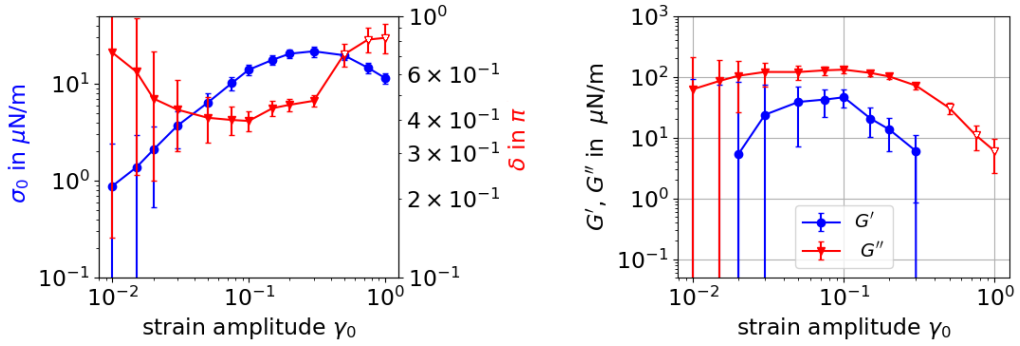

(a) stress amplitude σ_0 and phase lag δ (b) storage G' and loss G'' modulus

Figure 10: Results in a) stress amplitude σ_0, phase lag δ and b) viscoelastic moduli G', G'' of an amplitude sweep at frequency $f = 0.125\,\mathrm{Hz}$. Hollow markers indicate nonlinear cases with manual calculation of δ.

Firstly, as δ is larger than $\pi/2$ outside of the mentioned interval and it depends on $\sin(\delta)$, the storage modulus G' is negative. Therefore it can not be displayed on a logarithmic scale.
Secondly, the elastic component G' is always smaller than the viscous G'', meaning the network classifies as **liquid-like** over the whole range of strain. G'' displays a plateau up to a yield strain of $\gamma_L \approx 0.1$. Beyond that point it drops off toward 0. G' follows the same trend above the yield point. However, it also decreases going to smaller strain, assuming a maximum there. A plateau at low strain could be

considered within the interval of uncertainty.
Two other amplitude sweeps are run for frequencies $f = 0.4\,\mathrm{Hz}$ and $f = 0.04\,\mathrm{Hz}$. The resulting graphs of the viscoelastic moduli are depicted in fig. 11.

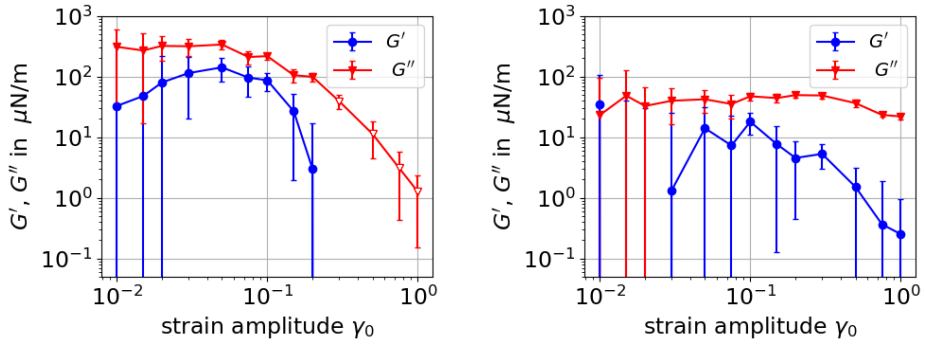

(a) $f = 0.4\,\mathrm{Hz}$ (b) $f = 0.04\,\mathrm{Hz}$

Figure 11: Storage G' and loss modulus G'' for strain amplitude sweeps for two separate frequencies f given below graph. Hollow markers indicate calculation of δ.

At $f = 0.4\,\mathrm{Hz}$, the moduli qualitatively show a similar course to those of the previously discussed sweep. The yield point is not as easily visible, but possibly at a slightly smaller value. The plateau in G'' and maximum in G' are about three times as high as before. On the other hand for $f = 0.04\,\mathrm{Hz}$, the moduli are at much lower values. The loss modulus does not drop significantly in the swept strain range and the course of the storage modulus is very irregular. A discrete yield strain can not be made out, but may be considered in the interval $\gamma_L \in [0.1, 0.5]$. This irregular and diminished response may result from the period of deformation being much larger than the internal dynamics on the scale of the swept amplitudes.

To better compare the differences between the sweeps, G' and G'' are also illustrated individually for the different frequencies, see fig. 12. It is visible that the approximate yield point decreases with larger frequency, while the magnitude of both moduli increases. Thus the extent of the LVER is frequency dependent. It is also seen for every frequency that G' decreases above, but also below the yield point. Below $\gamma_0 \approx 0.05$ errors become large. With this in consideration the strain amplitudes chosen to execute frequency sweeps at are $\gamma_0 \in \{0.05, 0.1, 0.2\}$.

Regarding the types of viscoelastic responses as characterized by Hyun *et al.* **laos**, these results are best categorized as **strain thinning**. However, there is the curved shape of the G' dependence, instead of a an expected plateau. This can not be simply assumed to be reflective of systems properties as it carries high uncertainty, but the fact that it shows for all sweeps, with multiple simulations each, gives it some validity. As explained in section 2.5.3, a model was found that exhibits an elastic overshoot after the yield point. Considering two cells attached through pili are very close to such a bead-spring dumbbell, a similar response to shear is not unlikely. However, below the yield point this model has a regular plateau in both moduli, which can not be seen in our results, possibly indicating another type of

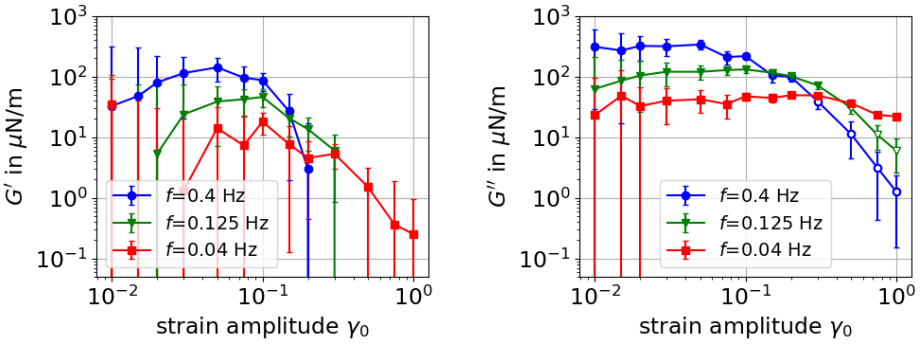

(a) Storage modulus G' (b) loss modulus G''

Figure 12: Components of dynamic modulus a) G' and b) G'' for strain amplitude sweeps at three separate frequencies f. Hollow markers indicate manual calculation of δ.

LAOS response.

4.3.2 Frequency sweeps

The swept frequency range is set to be $f = [0.0125\ \text{Hz}, 8\ \text{Hz}]$. First the results of a sweep at $\gamma_0 = 0.1$ are discussed. Stress amplitude σ_0 and phase lag δ are depicted in fig. 13(a).

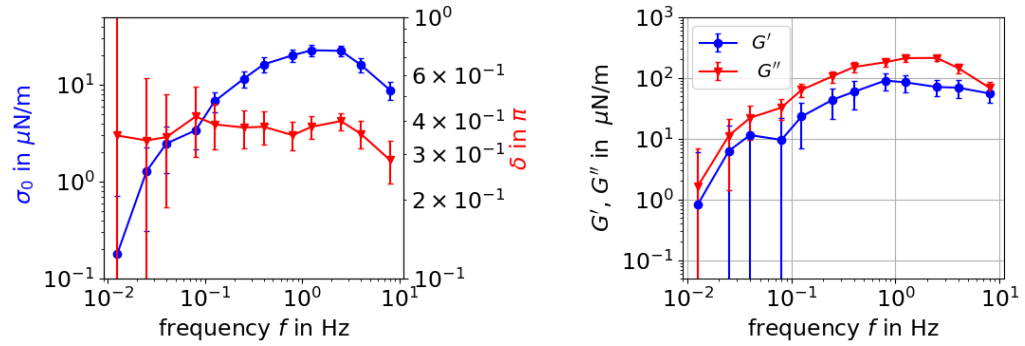

(a) stress amplitude σ_0 and phase difference δ (b) storage G' and loss G'' moduli

Figure 13: Results in a) stress amplitude σ_0, phase lag δ and b) viscoelastic moduli G', G'' of a frequency sweep at strain amplitude $\gamma_0 = 0.1$

Over most of the frequency range, the phase lag stays approximately constant. There are some local features that stay within the range of uncertainty. However, they can also be seen for a frequency sweep at $\gamma_0 = 0.05$, which might validate them as features. For small frequencies the errors become very large, being a similar case as in fig. 8(a)
The stress increases with frequency up to about $\approx 1.25\,\text{Hz}$. Above that point, stress

and phase difference fall off. Here the response becomes increasingly nonlinear. Thus the viscoelastic moduli follow a very similar course as the stress amplitude over most of the range, see fig. 13(b). G' and G'' increase with frequency up to a maximum after which they fall off. The elastic component takes its maximum slightly before the viscous.
The same description is valid in a frequency sweep at $\gamma_0 = 0.05$, see fig. 14(a). A larger strain of $\gamma_0 = 0.2$ only produces a similar trend up to its maximum at 0.25 Hz, fig. 14(b). At higher frequencies both moduli decrease rapidly and the response becomes nonlinear. Like before, the resulting elastic modulus is smaller than 0, not being visible in the graph.

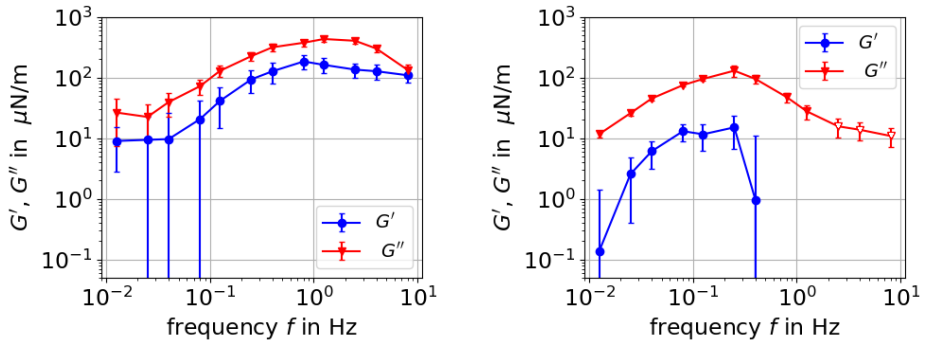

(a) $\gamma_0 = 0.05$ (b) $\gamma_0 = 0.2$

Figure 14: Viscoelastic moduli G' and G'' over frequency for frequency sweeps for strain amplitudes γ_0 given below respective graph. Hollow markers indicate manual calculation of δ.

Comparing the frequency sweeps for each modulus individually, see fig. 15, it is apparent that both components are qualitatively almost identical for the smaller strain amplitudes. They only differ slightly in magnitude and at very small frequencies, the latter being within the tolerance of the errors. This supports the suggestion that these strain amplitudes are within the LVER. At $\gamma_0 = 0.2$ this is not the case anymore, as the course of the moduli is differs significantly. Still, given that it is partially in line with the others and only then trails off, supports the suggestion that this strain is slightly above the yield point. Thus validating the assumption $\gamma_L \approx 0.1$.

With regard to section 2.5.3, Townsend and Wilson [39] identified the frequency at which the elastic intersects the viscous modulus to be the inverse of the dumbbells relaxation time τ_r. In the attained results in this theses there is no such point. However, the intersection in [39] is incidental with a maximum of G''. Therefore we approximate the relaxation time with $1/f$ at the maximal G'' for the two sweeps inside the LVER. For both sweeps this lies between 1.25 Hz and 2.5 Hz.
We thus take the average $f_{max} = 1.9 \pm 0.6$ Hz, which yields $\tau_r \approx 0.5 \pm 0.2$ s. Another way to determine, but also envision the relaxation time, is as the characteristic time scale of the networks exponentially declining stress response after a step deformation is applied [33].
The determined τ_r is very small compared to a relaxation time in the order of min-

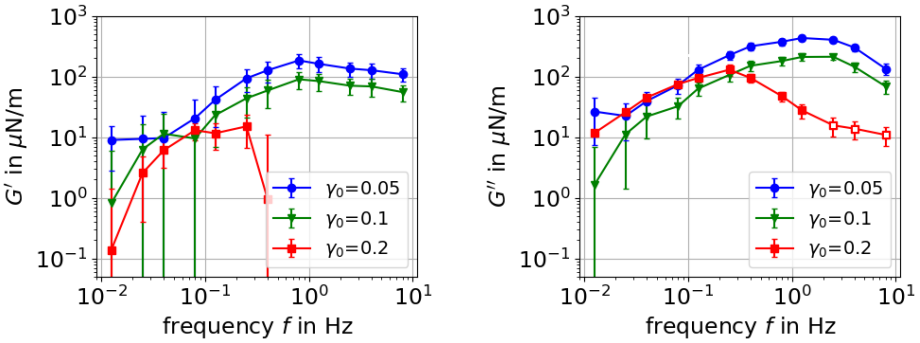

(a) Storage modulus G' (b) loss modulus G''

Figure 15: Components of dynamic modulus a) G' and b) G'' for frequency sweeps at three separate strain amplitudes γ_0. Hollow markers indicate manual calculation of δ.

Table 3: Peaks in G' within amplitude and frequency sweeps

f in Hz	0.125	0.25	0.4	0.8	0.8
γ_0	0.1	0.2	0.05	0.05	0.1
T in s	8	4	2.5	1.25	1.25
Δs in μm	0.7	1.4	0.35	0.35	0.7

utes found for bacterial biofilms [7]. Although the actual values of results in this thesis do not have claim for physical relevance, a disparity between biofilms and microcolonies in this regard is not unlikely nontheless. Bacteria in biofilms are less motile and reside in an extracellular matrix, increasing structural stability. On the other hand, the colony in this model constantly rebuilds its elastic network and rearranges due to the active pili interaction.

The apparent maxima of the elastic modulus G' that occur in these frequency sweeps are a peculiar feature, as no similar results were found in the research for this thesis. They may be interpreted as a resonant response of internal dynamics to the strain, similar to the viscous maximum in the bead-spring dumbbells marking the relaxation time, see section 2.5.3. For the elasticity to be maximal, the wall motion has to correspond to some time and length scale of the network dynamics or locate the intersection of two competing effects.
In table 3 the locations of all unambiguous maxima in G' are listed. Those tuples (γ_0, f) are determined from the amplitude sweeps as well as the frequency sweeps, see figs. 12(a) and 15(a). These are then converted to values of period T and displacement Δs, to attain associated measures of time and length. Errors are determined with the difference to the neighboring data points in the sweep. Thus those from amplitude sweeps have errors in length and those from frequency sweeps in time. They are not given in the table for clarity.

To compare this with the internal dynamics of the unperturbed network, they are plotted together with the correlation times τ in dependence of distance threshold d as per the OCF, values given in table 2. Fig. 16 shows the resulting graph in a double logarithmic plot.

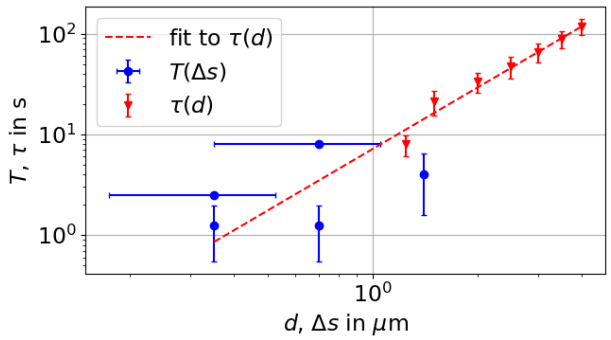

Figure 16: Time over length measures determined from the overlap correlation function $\tau(d)$, and through maxima of the elastic modulus $T(\Delta s)$ in the amplitude (x-error) and frequency sweeps (y-error).

The OCF yields data that decently follows a power law, being approximately on a straight line in the graph. It is fitted with a mononomial $\tau(d) = \alpha d^{\beta}$, which is extrapolated. Fit parameters are not given, as the exact function is not of importance. On the contrary, the data retrieved through elastic maxima $T(\Delta s)$ does not have a clear dependence. However, the values are scattered around the extrapolation of the function fitted to $\tau(d)$. This may imply that simply from the diffusive dynamics of a network viscoelastic properties can be inferred. Validation that this is feasible may be given by Dasgupta *et al.* [38], who proposed a method of determining storage and loss modulus from the MSD through a Laplace transform.

4.4 Nonlinear response

In this section we have a closer look at the anomalous stress responses that occur at the edges of sweeps, briefly presented before in fig. 8. The aim is to gain further understanding what causes this behaviour.
There are two types of deviation in the wall force from the expected, linear response. One shows strong fluctuations in its course and the other a distinct curve that is not sinusoidal, showing nonlinearity. Similar to the previous section, for each sweep the parameters (γ_0, f), at which those phenomena visibly prevail are approximately located. Fig. 17 illustrates the dependence of γ_0 over f in a double logarithmic plot. Therein, the data roughly lies on a straight line for both types respectively. Thus it is found, that the product $\gamma_0 \cdot f$, marking the approximate onset of said behaviour, is within reason of being constant. The region between these borders is where the network exhibits a defined linear response. For reference, the location of the elastic maxima in G' from the previous section are also plotted, without errors for clarity. They reside within the established borders, but close to them in some cases.

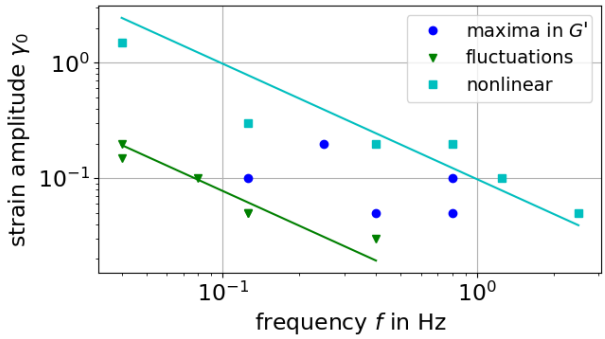

Figure 17: Tuples of strain amplitude γ_0 and f, at which anomalous stress response become prevalent in sweeps. The solid line represents the average of $\gamma_0 \cdot f$ for each type.

Strongly fluctuating stress, like in fig. 8(a), occurs below $\gamma_0 f = 8 \pm 2\,\mathrm{mHz}$. When converting γ_0 back to the wall displacement Δs, the corresponding product can be seen as a velocity $v_{fluc} = f\Delta s \approx 0.05\,\mu\mathrm{m/s}$. This is ten times slower than the average cell velocity $\overline{v}$ in the steady state, as illustrated in fig. 5(b).
Thereby, the explanation that this effect is caused by the active cell dynamics being much faster than the deformation is affirmed. Furthermore, relating this velocity to the relaxation time yields $\tau_r \cdot v_{fluc} \approx 0.03\,\mu\mathrm{m}$. This might be interpreted as applying a step deformation smaller than this value producing no apparent internal stress.

Concerning **nonlinear stress curves**, a border region of $\gamma_0 f = 0.1 \pm 0.04\,\mathrm{Hz}$ is found. Above, a behaviour akin to than in fig. 8(b) manifests. Here the corresponding velocity $v_{nl} = 0.7 \pm 0.4\,\mu\mathrm{m/s}$ is in the same order of magnitude as the cell velocities $\overline{v}$ and v_{exp} from fig. 5(b).
With respect to fig. 9, it is suspected that the nonlinearity is connected to the strain rate. Thus nonlinear curves of similar strain rate amplitude $\dot{\gamma}_0 = 2\pi f \gamma_0$ are

compared. The variable tuples $(\gamma_0,\ f)$ of chosen example cases lie in the upper range of the three frequency sweeps and are specifically :
Case 1: (0.058, Hz) **Case 2:** (0.1, 4 Hz) **Case 3:** (0.2 2.5 Hz)
Their respective period-averaged wall force is illustrated in fig. 18.

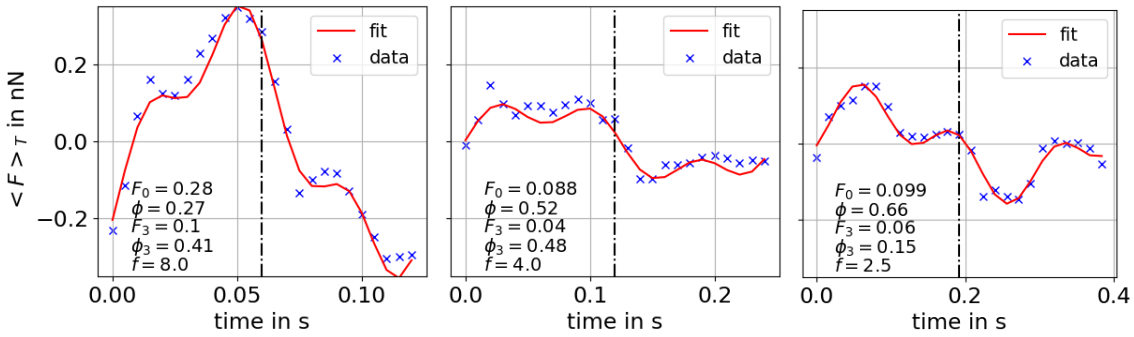

(a) $\gamma_0 = 0.05$ (b) $\gamma_0 = 0.1$ (c) $\gamma_0 = 0.2$

Figure 18: Period averaged wall force $\langle F_T \rangle$ and fitted function of form (42) with parameters given in graph.

All graphs show similar curves, in the way that the extrema of the sinusoidal response are superimposed with a sort of double peak. Yet they vary in the regard toward which shoulder it is tilted.
In case 1 it is tilted backwards, toward the second maximum. Case 2 shows maxima of about the same height and in case 3 the first is larger. The latter also has a more pronounced double peak, which may in part be explained by a slightly larger $\dot{\gamma}_0$ than the other cases. Respectively for each case, other frequencies in the same sweep with visible nonlinear curves share these qualities.
To quantify the nonlinear response, a curve of the form (42) is fitted to the data. Here a third harmonic contribution of different phase shift is added to the linear response, which can be seen as a Fourier series expansion to the next non-vanishing term. There are no even contributions, since the imposed strain is odd [37]. Resulting curve and fit parameters are given in fig. 18. Errors are not displayed for clarity. This form encompasses the data well, up to some edgy features.

$$F = F_0 \sin(2\pi f + \phi\pi) + F_3 \sin(2\pi 3 f + \phi_3 \pi) \tag{42}$$

The varying qualities of the curves for the three cases are a result of the difference in ϕ and ϕ_3. In case 1 ϕ is smaller than ϕ_3, while they are about the same in case 2 and case 3 has $\phi > \phi_3$. To eliminate time dependence and magnitude of response, a comparative Lissajous-Bowditch plot is looked at, where stress and strain are normalized with respect to their amplitude. It is depicted in fig. 19(a). Only the graphs for case 1 and 3 are shown, once for clarity and because 2 is an intermediate stage.

They show a very similar shape, again with case 3 being slightly more curved. However, they are tilted with respect to each other. In both cases the temporal development of stress and strain is clockwise along the shape.
Also the dependence of normalized stress over strain rate is looked at, see fig. 19(b).

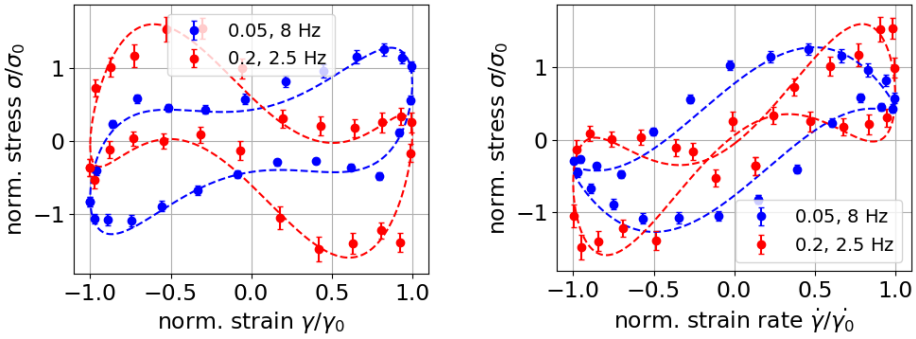

(a) stress over strain

(b) stress over strain rate

Figure 19: Lissajous-Bowditch plots of normalized stress over a) strain and b) strain rate for nonlinear responses with corresponding variable tuples (γ_0, f) given in legend. The markers represent the data and the dashed line a fit of form eq. (42). Fit parameters can be seen in respective graphs in fig. 18.

Here their shapes differ more, but they seem to be aligned. The common axis is approximately the diagonal $\sigma/\sigma_0 = \dot{\gamma}/\dot{\gamma_0}$, meaning their response can be considered as being in phase with the shear rate. This indicates the nonlinearity to be a viscous effect.
The difference in shapes is largely explained by the more pronounced indent between the peaks in case 3, see fig 18(c). This is quantified by the amplitude ratio F_3/F_0, which is significantly larger in case 3. A strain rate dependent nonlinearity produces this, because the linear elastic contribution is proportional to γ_0. Therefore the amplitude of the viscous becomes larger in relation, when γ_0 decreases, but $\dot{\gamma_0}$ stays constant.
When the shape is accounted for, the only remaining difference between case 1 and 3 is the direction of temporal stress-strain development. In case 1 it is still clockwise, while in case 3 it is anti-clockwise now. This results from the tilt of the shapes in fig. 19(a) being positive for case 1 and negative in case 3.
Hyun *et al.* classified nonlinear responses of form eq. (42) with respect to the phase angle $\delta_3 = \phi_3\pi$ and the coefficient sign of the third-order contribution, here F_3. Case 1, 2 and 3 all fall into the category of $0 < \delta_3 < \pi/2$ and $F_3 > 0$, which is titled as a **Viscous Nonlinearity**. This matches the previous suggestion.

Thus we have found the nonlinear effect to be viscous, as it is a function of shear rate rather than amplitude. Now it is also known, that nonlinear responses become relevant at deformations faster than the average cell velocity $v_{nl} \approx \overline{v}$. When the walls move faster than the characteristic cell speed, emergence of a nonlinear effect does not seem far fetched, especially considering the mechanism of pilus detachment due to force threshold F_{th}. This is supported by the earlier look at the networks attachment to the wall cells for such an example, see fig. 9. This active de- and reattachment at large strain rates may be considered a form of active wall slip, where cells in the colony regulate connections to those at the surface depending on their relative speed.

4.5 Impact of activity

The activity of this network causes interesting effects, such as the anomalous stress responses discussed above. Now it is investigated which features seen in analysis of amplitude and frequency sweeps might also stem from the model's active dynamics. To this end these results are compared to those of analogous passive network models. Therefore passive versions of the Ng-microcolony model, titled P1 and P2, are implemented. In the following their mechanism in comparison to that described in section 3.1 is briefly explained.

P1: Removing the source of activity, growth and attachment process for pili is stopped. Those that are not attached in the initial steady state are disregarded. The same is the case for pili that detach during the simulation.
Moreover, the detachment due to maximum duration T_{hold} is also removed. Otherwise there are no attractive connections after it has passed.

P2: The second passive model also fulfills these changes to the Ng-model. Additionally the detachment due to the force threshold F_{th} is removed. This distinction results in a vastly different outcome.

Those models were also subjected to an amplitude and frequency sweep with DMA. Fitting the stress curves had to be slightly adjusted.
P1 shows nonlinear curves in an even larger region than was found before, which may be explained by the elastic contribution being smaller (see below) and therefore a viscous, nonlinear effect being even more dominant. However, it is of different quality than those discussed in the previous section and may be compared to a sinusoidal with the maxima squeezed into a more narrow shape. This difference to the active model is likely due to another mechanism being its cause, since here there are peaks close to maximum strain rate, while before there were indents. To still determine the approximate linear viscoelastic response, fits of the nonlinear form are used and then only the first harmonic contribution is taken for further calculation, see eq. (42). Again, the stress curves are well approximated by this function.
For P2 the stress is neatly sinusoidal for all simulations, but it has a y-offset. This may be explained by an existing tension in the initial state for $\gamma = 0$. Here simply a constant was added to eq. 33 for the fitting function.
With this, storage and loss modulus are then calculated for both passive models. The results of an amplitude sweep at frequency $f = 0.125\,\mathrm{Hz}$ are depicted in fig. 20. As reference, the result of the active model is also given.

P2 has an almost constant course of G' and G''. They only decrease very slightly over the swept range and G' is always larger than G''. Hence the network entirely categorizes as solid-like. This can be expected, as the elastic connections in the network are ideal and do not break, leading to the material experiencing no yield.
On the other hand, P1 categorizes as liquid-like with G'' being larger. The moduli already have smaller values at the start of the strain range than for P2 and then even decline exponentially with γ_0. Extrapolation of the trend in G' toward smaller strain both models suggest an intersection at about $\gamma_0 \approx 0.003$. The associated

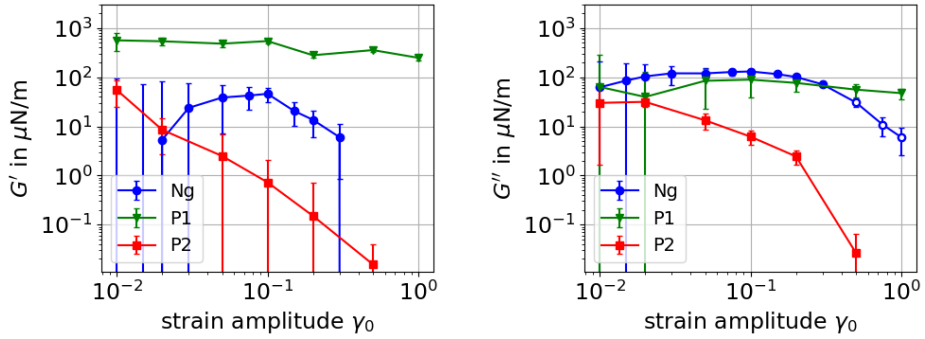

(a) Storage modulus G' (b) Loss modulus G''

Figure 20: Viscoelastic moduli from an amplitude sweep at $f = 0.125\,\text{Hz}$ for the Ng-model (Ng), a passive model with (passive 1) and without (P2) force threshold detachment of pili. Hollow markers indicate manual calculation of δ.

length $\Delta s \approx 0.021\,\mu\text{m}$ is close to the maximum elongation a pilus can experience $\max(\Delta L) = \frac{F_{th} - F_p}{k_{pil}} = 0.02\,\mu\text{m}$, see eqs. (14) and (19). This agrees with the notion, that for extremely small amplitudes shearing should not break any pili-bonds in P1. Therefore both passive models would have the same network of interactions, resulting in equal viscoelastic properties. With increasing strain amplitude then P1 loses connections successively, decreasing the elastic stress. Also wall slip becomes more prevalent.

The maximum of the active model's elastic modulus G' is right in between those of the passive models of same strain. Whereas for G'' it is larger than that of both other curves up to about its yield point. While all models show some degree of strain thinning, neither P1 nor P2 have a maximum in G' like the active. Therefore it may indeed be a result of resonance to the activity.
Comparison of the active and passive models' frequency sweeps can be seen in fig. 21. They are executed at a strain amplitude of $\gamma_0 = 0.05$. Here P1 and P2 behave qualitatively similar, in the expected manner of an ideal viscoelastic material, explained in section 2.5. Again, P1 produces moduli of much smaller values, which become irregular and error ridden toward large frequencies. Still a steady increase in the trend of storage and loss modulus with frequency can be made out.
The same is true for P2 in G'', while it only holds for G' above a certain frequency. Below, the elastic component stays approximately constant. The transition occurs in about at the frequency, at which the active model assumes its maximum. This may be traced back to the relaxation time, as the corresponding frequency is close to the region of changing slope. When the deformation is slower than the relaxation time of elastic connections the resulting deformation may be considered steady-state like. At shear periods smaller than the relaxation time, the spring like connections are extended more, since the cells do not rearrange as quickly as the deformation occurs. Thus the elastic stress and therefore G' increase with frequency. Active model and P1 do not show this course in G', because the effect is diminished through the force threshold detachment and hence other factors are represented in their response.

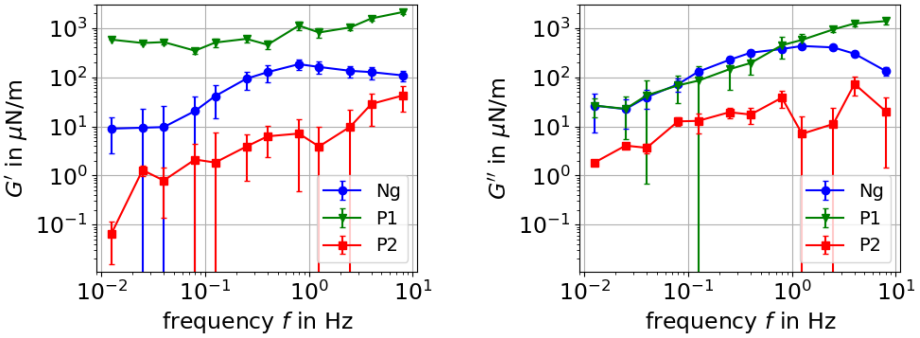

(a) Storage modulus G' (b) Loss modulus G''

Figure 21: Viscoelastic moduli from a frequency sweep at $\gamma_0 = 0.05$ for the Ng-model (Ng), a passive model with (P1) and without (P2) force threshold detachment of pili.

Again the elastic modulus of the active model lies in between those of the passive ones and the viscous modulus is larger up to a certain value. Here the point of the active G'' falling below that of P2 is approximately the location of the elastic maximum. The active moduli maxima are unique in comparison of these three models. For the bead-spring dumbbells from section 2.5.3, also being passive, a maximum in G'' but not in G' is observed. Once more the assumption, the elastic maxima are a feature of activity is reassured.

In a physical setting, an active material has to constantly convert potential into kinematic energy. Thus a system's degree of activity may be equated with its power consumption.
An increased activity of the Ng model means faster growth and retraction of pili and possibly larger pulling forces. This would likely result in a higher viscosity, as the cell bodies have a larger average velocity due to increased rate and strength of interaction. Since the network of elastic bonds then changes even more quickly, the relaxation time would decrease. Thus the maximum in G'' and likely also G' shifts to larger frequencies. Also a shortened lifespan of elastic connections may result in an overall decrease in elastic modulus. At the same time, the aggregating properties would likely be enhanced.
Reduced activity should consequently result in the opposite behaviour.
In recent investigation of active matter embedded in colloidal gels, it was also observed that elasticity decreases with energy relating to the activity [9].

4.6 Conclusions

It is shown that a model for a Ng microcolony has shear thinning properties. Concretely, elastic and viscous moduli G' and G'' decrease with larger amplitudes of shear deformation in amplitude sweeps. Approximate extent of the network's LVER is determinined by locating the yield strain at $\gamma_L \approx 0.1$. Although also uncertain, apparent behaviour of G' is uncommon, assuming a maximum but no plateau.
Frequency sweeps indicate a resonant viscoelastic response to shear, as all moduli take on a maximum. The relaxation time of the network is determined as $\tau_r \approx 0.5\,\mathrm{s}$, by relating it to the maxima of G'' for sweeps within the LVER.
Additionally, comparing time and length scales corresponding to all maxima in G' in both sweep types and diffusive measures of the steady state calculated with the OCF, suggests a correlation between them. Thus information about the approximate elastic resonance of a system may be obtained by looking at its diffusive behaviour.
The network's region of a clear, linear response to shear is found to be bound by constant products $\gamma_0 f$. Below the lower border, fluctuations through active cell motion overshadow the feedback to deformation. For large values of $\gamma_0 f$, the linear approximation of stress response does not suffice.
Nonlinear stress curves with a double peak are observed, that changes its tilt depending on the strain amplitude. This quality is well embraced by adding a third harmonic to the linear response. Different tilt thus results from the relative phases of linear and nonlinear stress. The nonlinearity is found to be strain rate dependent, therefore of viscous origin and likely due to active interaction with the wall.
With passive model variants of that for the Ng microcolony, the impact of activity onto the systems viscoelasticity is examined. Comparison shows that the active model maximizes viscosity and mitigates elasticity. Also, no elastic resonances in the form of maxima in G' are found for passive models. Therefore this seems to be a distinguished feature of an active model. It is presumed that increased activity would shift the elastic response to larger frequency and lower it overall.

Thus several interesting aspects of the Ng model revealed themselves. They are mostly based in the network's intrinsic activity.
The observed resonances in elasticity at high frequencies may point toward a viscoelastic protection mechanism bacterial microcolonies developed against displacement. It may imply an ability to absorb sudden and brief perturbations elastically, while extended stress loads are dissipated through flow, avoiding tearing the colony apart [7].
Furthermore, the viscous nonlinearity may be an extension of this behaviour, as it becomes prevalent just above elastic maxima. Active detachment at high strain rates could mean the colony letting go of cells that have gained momentum, thus mitigating losses by others being dragged along. On the other hand, it may also be the cause of the maxima, as elastic contribution is diminished by fewer connections to the wall.
More detailed investigation into and assurance of those effects may lead to discovery of novel viscoelastic properties for active networks and pilated bacteria. This may help in development of durable artificial active matter or treatment of harmful bacterial microcolonies, preventing formation of even more resilient biofilms.

5 Summary

In this thesis it was attempted to gain insight into the viscoelastic properties of an active network in the form of a Ng microcolony. Therefore, a partly new model for actively interacting Ng cells was numerically implemented.
Its use was qualitatively validated by reproducing relevant bacterial properties observed in experiments, namely twitching and clustering. The system's steady state was investigated regarding time scales of internal dynamics. Mean square displacement, velocity distribution and a two-point correlation function were used as tools.
Then the network's viscoelasticy was tested with oscillating shear deformation. Storage and loss modulus were calculated with the assumption of a linear response, by fitting a sinusoidal curve to the measured shear stress. Border cases of noisy data and nonlinear curves were pointed out and a way of integrating such results proposed.
Evaluating amplitude sweeps at different frequencies revealed the network to be liquid-like and have strain thinning properties. The LVER and yield point were approximately located. A curious course of the elastic modulus was found and attempted to be categorized.
Frequency sweeps were executed in the approximated LVER and thereby its limits checked. Maxima in the viscous modulus for SAOS were related to the networks relaxation time. Furthermore, the elastic modulus was also revealed to assume a maximum in the swept frequencies, indicating a resonant response.
Time and length scales obtained through all maxima of the storage modulus in amplitude and frequency sweeps were compared to those provided by the correlation function. It was surmised that diffusion and elastic resonance are closely related.
Cases of anomalous viscoelastic response and their occurrence were further investigated. The region of these fluctuating and nonlinear stress curves becoming prevalent was determined. Through analysis with a higher order harmonic contribution, the nonlinearity was quantified. Together with Lissajous-plots it was concluded, that the underlying mechanism is strain rate dependent wall attachment.
At last, the effect of the model's activity onto its viscoelastcity was looked into. Two passive model variants were implemented as comparison and the results of an amplitude and frequency sweep of all models compared. It was found that there are no dynamic resonances without activity. Additionally, the differences in viscoelastic response were taken as indication that the degree of activity increases the systems viscosity while presumably shifting and decreasing elastic response.

6 Outlook

In further study of this system, the following aspects may be considered to be added, to improve the model or make it more realistic.
Firstly, turning to a three dimensional model is clearly closer to a physical system. Secondly, simulating a larger system will enhance the results, as it provides more statistical security. For instance at small strain amplitudes the large errors seen in this thesis may in part stem from wall displacements smaller than the diameter of a single cell and are therefore very sensitive to initial conditions. For a larger box and the same amplitude this may not be the case.
A further analysis of the degree of activity on the viscoelasticity might be interesting. Active colloids are often modeled embedded in passive solutions for rheologic tests [9] [11] [10] and there has already been some investigation into other aspects of Ng colonies with cells of different pilus-activity [27].
Instead of pure amplitude and frequency sweeps, systems with such complex responses to shear may be tested on a grid of frequencies and amplitudes. Storage and loss moduli could then be displayed as a heat map and features, such as extrema, globally evaluated.
Regarding Ng specifically, as the cells appear as diplococci they are often modeled as two overlapping spheres [41][27]. Then also torque and rotation should be implemented, since the cell isotropy is broken. This will add effects stemming from cell alignment, as it also is a source of other recent discoveries for elongated bacteria with TFP [20][21].
Another aspect which may have a considerable impact on the rheological properties is *pili bundling*, which is a phenomenon observed for Ng. It describes the mechanism of up to 8-10 pili coordinating to form retractable units, which are proportionally stronger and more durable than the individual [43][31].
Implementing these changes provides a more powerful model, with which the understanding of active bacterial adhesion might be expanded, possibly helping in counteracting or reproducing such effects in real world settings.

7 Abbreviations

- DMA Dynamic mechanical analysis, section 2.5
- LVER Linear viscoelastic region, section 2.5
- LAOS Large amplitude oscillatory shear, section 2.5
- MSD Mean square displacement, section 3.3.1
- Ng Neisseria gonorrhoeae, section 2.2
- OCF Overlap correlation function, section 3.3.2
- SAOS Small amplitude oscillatory shear, section 2.5
- TFP Type IV pili, section 2.3

List of Figures

List of Tables

References

[1] D. L. Higashi, S. W. Lee, A. Snyder, N. J. Weyand, A. Bakke, and M. So, "Dynamics of Neisseria gonorrhoeae attachment: Microcolony development, cortical plaque formation, and cytoprotection," *Infection and Immunity*, vol. 75, Oct. 2007.

[2] J. Mattick, "Type iv pili and twitching motility," *Annual review of microbiology*, vol. 56, Feb. 2002.

[3] L. Johnson, "Microcolony and biofilm formation as a survival strategy for bacteria," *Journal of theoretical biology*, vol. 251, Apr. 2008.

[4] X. Wang, K. ZHAO, and H. ZHAO, "Finite element simulation of biofilm viscoelastic behavior under various loadings," *Journal of Mechanics in Medicine and Biology*, vol. 18, Aug. 2018.

[5] P. Barai, A. Kumar, and P. P. Mukherjee, "Modeling of mesoscale variability in biofilm shear behavior," *PLOS ONE*, vol. 11, no. 11, Nov. 2016.

[6] E. Gloag, S. Fabbri, D. Wozniak, and P. Stoodley, "Biofilm mechanics: Implications in infection and survival," *Biofilm*, vol. 2, Dec. 2019.

[7] I. Klapper, C. Rupp, R. Cargo, B. Purvedorj, and P. Stoodley, "Viscoelastic fluid description of bacterial biofilm material properties," *Biotechnology and bioengineering*, vol. 80, Nov. 2002.

[8] S. Ebbens, "Active colloids: Progress and challenges towards realising autonomous applications," *Current Opinion in Colloid & Interface Science*, vol. 21, Oct. 2015.

[9] M. Szakasits, K. Saud, X. Mao, and M. Solomon, "Rheological implications of embedded active matter in colloidal gels," *Soft Matter*, vol. 15, Sep. 2019.

[10] G. Foffano, J. S. Lintuvuori, K. Stratford, M. E. Cates, and D. Marenduzzo, "Dynamic clustering and re-dispersion in concentrated colloid-active gel composites," *Soft Matter*, vol. 15, 2019.

[11] A. Patteson (Koser), A. Gopinath, and P. Arratia, "Active colloids in complex fluids," *Current Opinion in Colloid & Interface Science*, vol. 21, Feb. 2016.

[12] M. Szakasits, K. Saud, X. Mao, and M. Solomon, "Rheological implications of embedded active matter in colloidal gels," *Soft Matter*, vol. 15, Sep. 2019.

[13] L. L. Greiner, J. L. Edwards, J. Shao, C. Rabinak, D. Entz, and M. A. Apicella, "Biofilm formation by Neisseria gonorrhoeae," *Infection and Immunity*, vol. 73, Apr. 2005.

[14] I. Ehrhard, "Neisseria gonorrhoeae," in *Lexikon der Infektionskrankheiten des Menschen : Erreger, Symptome, Diagnose, Therapie und Prophylaxe*, 3rd ed. Berlin, Heidelberg: Springer, 2009, pp. 580–586.

[15] P. Laniewski, A. Gomez, G. Hire, M. So, and M. Herbst-Kralovetz, "Human three-dimensional endometrial epithelial cell model to study host interactions with vaginal bacteria and Neisseria gonorrhoeae," *Infection and immunity*, vol. 85, Jan. 2017.

[16] D. C. Stein, "The Neisseria," in *The Prokaryotes: Volume 5: Proteobacteria: Alpha and Beta Subclasses*. Springer New York, 2006, pp. 602–647.

[17] L. Burrows, "Weapons of mass retraction," *Molecular microbiology*, vol. 57, Sep. 2005.

[18] T. Proft and E. Baker, "Pili in gram-negative and gram-positive bacteria—structure, assembly and their role in disease," *Cellular and molecular life sciences : CMLS*, vol. 66, Nov. 2008.

[19] R. Marathe, C. Meel, N. Schmidt, L. Dewenter, R. Kurre, L. Greune, M. A. Schmidt, M. Mueller, R. Lipowsky, B. Maier, and S. Klumpp, "Bacterial twitching motility is coordinated by a two-dimensional tug-of-war with directional memory," *Nature communications*, vol. 5, May 2014.

[20] K. Copenhagen, R. Alert, N. Wingreen, and J. Shaevitz, "Topological defects induce layer formation in Myxococcus xanthus colonies," *Nature Physics*, Nov. 2020.

[21] O. J. Meacock, A. Doostmohammadi, K. R. Foster, J. M. Yeomans, and W. M. Durham, "Bacteria solve the problem of crowding by moving slowly," *Nature Physics*, Nov. 2020.

[22] J. Skerker and H. Berg, "Direct observation of extension and retraction of type IV pili," *Proceedings of the National Academy of Sciences of the United States of America*, vol. 98, Jul. 2001.

[23] L. Craig, K. Forest, and B. Maier, "Type iv pili: Dynamics, biophysics and functional consequences," *Nature Reviews Microbiology*, vol. 17, Apr. 2019.

[24] B. Maier, L. Potter, M. So, C. Long, H. Seifert, and M. Sheetz, "Single pilus motor forces exceed 100 pn," *Proceedings of the National Academy of Sciences of the United States of America*, vol. 99, Jan. 2003.

[25] S. G. V. Charlton, M. A. White, S. Jana, L. E. Eland, P. G. Jayathilake, J. G. Burgess, J. Chen, A. Wipat, and T. P. Curtis, "Regulating, measuring, and modeling the viscoelasticity of bacterial biofilms," *Journal of Bacteriology*, vol. 201, Jun. 2019.

[26] J. Wilking, T. Angelini, A. Seminara, M. Brenner, and D. Weitz, "Biofilms as complex fluids," *MRS Bulletin*, vol. 36, May 2011.

[27] W. Pönisch, C. A. Weber, G. Juckeland, N. Biais, and V. Zaburdaev, "Multiscale modeling of bacterial colonies: How pili mediate the dynamics of single cells and cellular aggregates," *New Journal of Physics*, vol. 19, Jun. 2017.

[28] W. Pönisch, K. Eckenrode, K. Alzurqa, H. Nasrollahi, C. Weber, V. Zaburdaev, and N. Biais, "Pili mediated intercellular forces shape heterogeneous bacterial microcolonies prior to multicellular differentiation," *Scientific Reports*, vol. 8, Nov. 2018.

[29] A. Persat, C. Nadell, M. Kim, F. Ingremeau, A. Siryaporn, K. Drescher, N. Wingreen, B. Bassler, Z. Gitai, and H. Stone, "The mechanical world of bacteria," *Cell*, vol. 161, May 2015.

[30] V. Preda and O. Sandulescu, "Communication is the key: Biofilms, quorum sensing, formation and prevention," *Discoveries*, vol. 7, Sep. 2019.

[31] J. Taktikos, Y. T. Lin, H. Stark, N. Biais, and V. Zaburdaev, "Pili-induced clustering of N. gonorrhoeae bacteria," *PLOS ONE*, vol. 10, Sep. 2015.

[32] N. Biais, B. Ladoux, D. Higashi, M. So, and M. Sheetz, "Cooperative retraction of bundled type IV pili enables nanonewton force generation," *PLoS biology*, vol. 6, May 2008.

[33] T. G. Mezger, *The rheology handbook*, 4th ed. Hannover: Vincentz Network, 2014.

[34] J. D. Ferry, "Viscoelastic properties of polymer solutions," *J. Res. Natl. Bur. Stand.*, vol. 41, Jul. 1948.

[35] M. Unterberger, K. Schmoller, C. Wurm, A. Bausch, and G. Holzapfel, "Viscoelasticity of cross-linked actin networks: Experimental tests, mechanical modeling and finite element analysis.," *Acta biomaterialia*, vol. 9, Mar. 2013.

[36] P. Coussot, *Rheometry of Pastes, Suspensions, and Granular Materials*, 1st ed. Hoboken: John Wiley & Sons, Ltd, 2005.

[37] K. Hyun, M. Wilhelm, C. O. Klein, K. S. Cho, J. G. Nam, K. H. Ahn, S. J. Lee, R. H. Ewoldt, and G. H. McKinley, "A review of nonlinear oscillatory shear tests: Analysis and application of large amplitude oscillatory shear (laos)," *Progress in Polymer Science*, vol. 36, 2011.

[38] B. R. Dasgupta, S.-Y. Tee, J. C. Crocker, B. J. Frisken, and D. A. Weitz, "Microrheology of polyethylene oxide using diffusing wave spectroscopy and single scattering," *Phys. Rev. E*, vol. 65, May 2002.

[39] A. K. Townsend and H. J. Wilson, "Small- and large-amplitude oscillatory rheometry with bead–spring dumbbells in stokesian dynamics to mimic viscoelasticity," *Journal of Non-Newtonian Fluid Mechanics*, vol. 261, Sep. 2018.

[40] P. G. Jayathilake, B. Li, P. Zuliani, T. Curtis, and J. Chen, "Modelling bacterial twitching in fluid flows: A cfd-dem approach," *Scientific Reports*, vol. 9, Dec. 2019.

[41] V. Zaburdaev, N. Biais, M. Schmiedeberg, J. Eriksson, A.-B. Jonsson, M. Sheetz, and D. Weitz, "Uncovering the mechanism of trapping and cell orientation during Neisseria gonorrhoeae twitching motility," *Biophysical journal*, vol. 107, Oct. 2014.

[42] S. Chakrabarty, S. Karmakar, and C. Dasgupta, *Dynamics of glass forming liquids with randomly pinned particles*, Jul. 2015.

[43] C. Meel, D. Opitz, L. Greune, R. Kurre, M. Koomey, M. A. Schmidt, and B. Maier, "Multiple pilus motors cooperate for persistent bacterial movement in two dimensions," *Physical review letters*, vol. 104, Apr. 2010.

Acknowledgements

Since there were some hardships and delays in the writing of this thesis,
I want to thank my supervisor, Prof. Dr. Michael Schmiedeberg,
as well as my boss, Dr. Stefan Reinheimer,
for their support and patience.

Statutory declaration

I hereby confirm that I have written the accompanying thesis by myself, without contributions from any sources other than those cited in the text. This thesis was not submitted to any other authority to achieve an academic grading and was not published elsewhere.

Leander Self (Enrollment-No. 22375446)

Place, date : *Signature* :